CHAPTER

9

Larger Proteins and Molecular Interactions

A hallmark of the historical development of biological NMR spectroscopy is the continued increase in the size of the molecular species amenable to investigation. The first part of this chapter presents methods for resonance assignments and structure determination applicable to proteins with molecular masses of >20–30 kDa. These techniques are modifications of the experiments presented in Chapter 7 for smaller proteins. Increases in the size limits for solution NMR spectroscopy also facilitate investigation of molecular interactions and complex formation by proteins. The second part of this chapter discusses some of the many NMR techniques for detecting and quantifying intermolecular interactions between proteins and ligands. Efficiency in data acquistion remains an important concern. The final part of this chapter briefly discusses emerging methods for recording spectral data more rapidly.

9.1 Larger Proteins

The multidimensional triple-resonance NMR techniques described in Chapter 7 allow characterization of proteins up to a molecular mass

of ~20–30 kDa. In addition to the resolving power afforded by multiple frequency dimensions, the central premise behind such experiments is that transfer of magnetization occurs much more efficiently through large heteronuclear scalar couplings and ^{13}C–^{13}C homonuclear couplings than through small ^{1}H–^{1}H homonuclear scalar couplings (Table 7.2). Concomitant short magnetization transfer periods are employed to maximize sensitivity by keeping transverse relaxation losses to a minimum. However, as molecular masses increase beyond 20 kDa, proteins become progressively more difficult to study by these established methods (*1–7*). The NMR spectra of larger proteins contain more resonances and, because of longer rotational correlation times and correspondingly faster transverse relaxation, these resonances have larger linewidths. Consequently, resonance congestion escalates rapidly with increased molecular size. Increased transverse relaxation rate constants also decrease overall sensitivity, because less magnetization survives through pulse sequence delays to be detected by the receiver. Accordingly, for larger proteins, standard $^{13}C/^{15}N$-triple-resonance NMR experiments become ineffective. The following sections discuss approaches for overcoming these limitations [for a review, see Permi (*8*)].

9.1.1 PROTEIN DEUTERATION

Dramatically reducing the length of INEPT magnetization transfer periods, or other pulse sequence elements that rely on evolution under the scalar coupling Hamiltonian, in heteronuclear NMR experiments is not feasible, because delays of length $\sim 1/(2J_{IS})$ are required to ensure efficient coherence transfer from a given spin to its scalar-coupled partners (Sections 2.7.7.2 and 5.1.1). However, transverse relaxation rate constants can be reduced in larger proteins by eliminating (or avoiding) unfavorable relaxation pathways. The TROSY experiment discussed in Section 7.1.3 provides one illustration of this principle; the cross-relaxation-induced polarization transfer (CRIPT) technique uses relaxation interference rather than scalar coupling evolution to obtain coherence transfer (*9, 10*). Applications of optimal control theory to develop relaxation-optimized coherence transfer schemes are an active area of research (*11*).

Sensitivity of $^{13}C/^{15}N$ double- and triple-resonance NMR experiments used for assignment of protein backbone resonances is affected most adversely by increases in the transverse relaxation rate constants for ^{13}C and $^{1}H^{N}$ spins. The ^{1}H–^{13}C dipolar interaction dominates relaxation of ^{13}C spins for carbon atoms with directly attached hydrogen atoms (*12, 13*). Relaxation of $^{1}H^{N}$ spins has a

substantial component (~40%) arising from dipolar interactions with proximal aliphatic ^{1}H spins (*14*). Consequently, significant increases in both resolution and sensitivity can be realized by eliminating these specific relaxation pathways, thereby reducing R_2 for both ^{13}C and $^{1}H^{N}$ spins. This can be achieved by replacing most, if not all, carbon-bound hydrogen atoms in a protein with deuterium (^{2}H or D) (*15–22*).

The two labeling strategies in common usage are referred to as (*i*) *perdeuteration* and (*ii*) *random fractional deuteration*. Complete deuteration, or perdeuteration, replaces ~99% of all carbon-bound hydrogen atoms with deuterium atoms. Random fractional deuteration describes the distribution of deuterium throughout all protein molecules in the sample. For example, in a 70% randomly deuterated protein, on average over the entire sample, 70% of the protons have been replaced by deuterium, but not the same 70% in each molecule (*23–25*). In either case, proteins are produced biosynthetically by modifications of the overexpression protocols used to produce nondeuterated isotopically enriched proteins (*15, 26*). Perdeuterated proteins are obtained by growth of bacterial hosts on media containing perdeuterated carbon sources, such as perdeuterated [^{13}C] glucose or [99% ^{2}H, ^{13}C, ^{15}N] algal hydrolysate medium, in 99% D_2O solution. To first approximation, random fractional deuteration is achieved by simply expressing the protein in minimal media containing the appropriate v/v ratio of D_2O/H_2O (*14, 17, 20, 25*). Average enrichment levels of ~60–80% typically are obtained by growth on 99% D_2O with protonated glucose carbon sources. With this protocol, isotopic enrichment may not be completely random, and enrichment at the more acidic C^{α} carbon typically is higher than the average. Frequently, cell growth rates are significantly slower and protein expression levels are lower in D_2O solution. In addition, bacterial cells may require adaptation to growth in D_2O (*13*).

In distinction to either perdeuteration or random fractional deuteration, a third approach, termed SAIL (stereo-array isotope labeling), sterospecifically replaces ^{1}H atoms with ^{2}H atoms to provide optimal simplification of amino acid spin systems (*27*). This technique is highly promising, but not yet in general use. In some instances, biosynthetic metabolic pathways can be utilized to produce specified labeling patterns from labeled precursors added to growth media (Section 9.1.9) (*28–32*).

For either perdeuterated or random fractionally deuterated proteins, $^{1}H^{N}$ spins are reintroduced through amide proton solvent exchange by dissolving the protein in H_2O buffer. Reintroduction of $^{1}H^{N}$ spins is slow for amide moieties that are highly protected from solvent exchange and a reduction in sensitivity for these residues may

be observed. Unfolding of the protein to obtain complete exchange should be performed only if the subsequent refolding results in complete regeneration of the functional protein structure (*33*). For the purposes of the following discussion, $^{1}H^{N}$ spins are assumed to be fully present at all amide sites.

9.1.2 Relaxation in Perdeuterated and Random Fractionally Deuterated Proteins

Deuteration, when combined with $^{13}C/^{15}N$ isotopic labeling, produces a protein often referred to as *triply* labeled ($^{2}H/^{13}C/^{15}N$). Because the deuteron magnetogyric ratio (γ_D) is 6.5-fold smaller than the ^{1}H magnetogyric ratio (γ_H), a deuteron is $[I_H(I_H+1)/I_D(I_D+1)](\gamma_H/\gamma_D)^2 \sim 16$-fold less effective (where $I_H = 1/2$ and $I_D = 1$ are the spin quantum numbers of the ^{1}H and ^{2}H nuclei, respectively) than a proton at causing dipolar relaxation of the directly attached heteronucleus and surrounding ^{1}H nuclei. Figure 9.1 displays calculated T_2 relaxation times as a function of the rotational correlation time, τ_c, for backbone nuclei in both a fully protonated protein and its perdeuterated counterpart. The calculations include both CSA and dipolar contributions (*17, 34*). These calculations show that perdeuteration dramatically increases the T_2 ($= 1/R_2$) relaxation times for $^{13}C^{\alpha}$ (*13*) and $^{1}H^{N}$ (*14*) spins, but does not affect the T_2 relaxation of in-phase ^{15}N and ^{13}CO magnetization to significant extents. Figure 9.2 shows the average T_2 and T_1 relaxation times as a function of deuteration level for a protein with correlation time of 12 ns (at 600 MHz). The calculations include both CSA and dipolar contributions (*25*). The T_2 relaxation times of both $^{1}H^{N}$ and $^{1}H^{\alpha}$ spins increase with increasing level of random fractional deuteration, with $^{1}H^{N}$ T_2 showing a rapid increase for deuteration levels of $\sim$50% and above. At the same time, increases in $^{1}H^{N}$ T_1 are small up to a deuteration level of $\sim$80%.

These calculations suggest that "out-and-back" experiments, in which magnetization originates and is detected on the $^{1}H^{N}$ spin, will be effective for proteins that are $>50\%$ deuterated. Indeed, a 70% random fractionally deuterated protein was used to develop a suite of triple-resonance experiments for the backbone assignment of triply labeled proteins (*13*). Perdeuteration provides the largest increase in T_2 relaxation times and consequent enhanced sensitivity and resolution in $^{1}H^{N}$-detected $^{13}C/^{15}N$ triple-resonance correlation experiments, particularly for obtaining $^{1}H^{N}$, ^{15}N, $^{13}C^{\alpha}$, and ^{13}CO backbone and $^{13}C^{\beta}$ side chain assignments (*17, 22, 35–37*). Optimization of the recycle

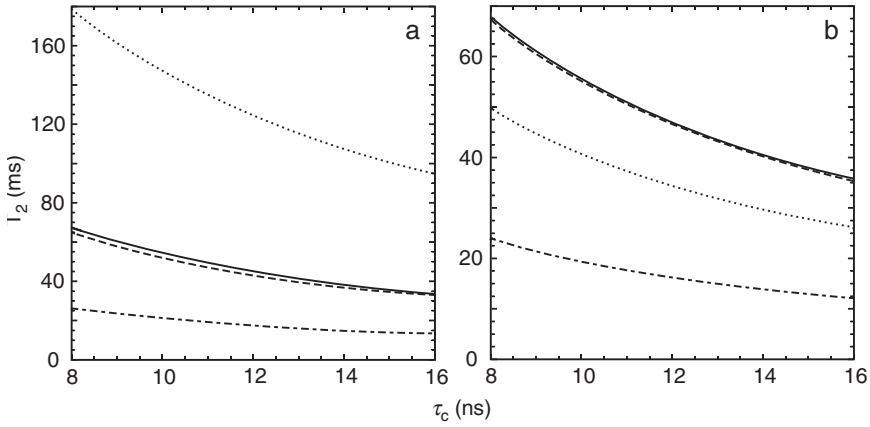

FIGURE 9.1 Calculated T_2 relaxation times versus the isotropic rotational correlation time for backbone nuclei in both a fully protonated protein (H) and its perdeuterated counterpart (D) (*17*). (a) (·····) $^{13}C^{\alpha}$(D), (-·-·-) $^{13}C^{\alpha}$ (H), (—) ^{13}CO(D), (- - - -) ^{13}CO(H). (b) (·····) $^{1}H^{N}$(D), (-·-·-) $^{1}H^{N}$(H), (—) ^{15}N(D), (- - - -) ^{15}N(H). The $T_2(^{15}N)$ relaxation times were calculated with the following parameters: $\Delta\sigma_N = -160$ ppm, $r_{N\text{-}HN} = 1.02$ Å, $r_{N\text{-}H^{\alpha}} = 2.12$ Å, $r_{N\text{-}CO} = 1.49$ Å, and $r_{N\text{-}C^{\alpha}} = 1.49$ Å. The $T_2(^{13}CO)$ relaxation times were calculated with the following parameters: $\Delta\sigma_{CO} = 102$ ppm, $r_{CO\text{-}C^{\alpha}} = 1.54$ Å, $r_{CO\text{-}N} = 1.49$ Å, $r_{CO\text{-}H^{\alpha}} = 2.16$ Å, and $r_{CO\text{-}HN} = (2.24$ Å, 3.30 Å). The $T_2(C^{\alpha})$ relaxation times were calculated with the following parameters: $\Delta\sigma_{C^{\alpha}} = 29.5$ ppm for Gly and 21.5 ppm for Ala, $r_{C^{\alpha}\text{-}D^{\alpha}} = 1.05$ Å, $r_{C^{\alpha}\text{-}H^{\alpha}} = 1.09$ Å, $r_{C^{\alpha}\text{-}H^{\beta}} = 2.16$ Å, $r_{C^{\alpha}\text{-}CO} = 1.54$ Å, $r_{C^{\alpha}\text{-}N} = 1.49$ Å, $r_{C^{\alpha}\text{-}C^{\beta}} = 1.54$ Å (Ala only), and $r_{C^{\alpha}\text{-}HN} = (2.24$ Å, 3.00 Å). The $T_2(^{1}H^{N})$ relaxation times represent an average of values from α-helices and parallel β-sheets. For an α-helix, each $^{1}H^{N}$ spin was assumed to interact with four other amide $^{1}H^{N}$ spins at the following distances: 2.8, 2.8, 4.2, and 4.2 Å. For a parallel β-sheet, each amide $^{1}H^{N}$ spin was assumed to interact with three other amide $^{1}H^{N}$ spins at the following distances: 4.2, 4.2, and 4.0 Å. In both cases, CSA contributions to the amide proton linewidth for a correlation time $\tau_c = 11.4$ ns were estimated at 3.8 Hz.

delay to reflect longer T_1 relaxation times may be necessary, particularly for perdeuterated proteins.

9.1.3 SENSITIVITY FOR PERDEUTERATED PROTEINS

For the gradient-enhanced, sensitivity-enhanced ^{1}H–^{15}N HSQC experiment (Section 7.1.4.2), the theoretical increase in sensitivity, S_r(D/H), due to perdeuteration, is calculated, using transfer functions

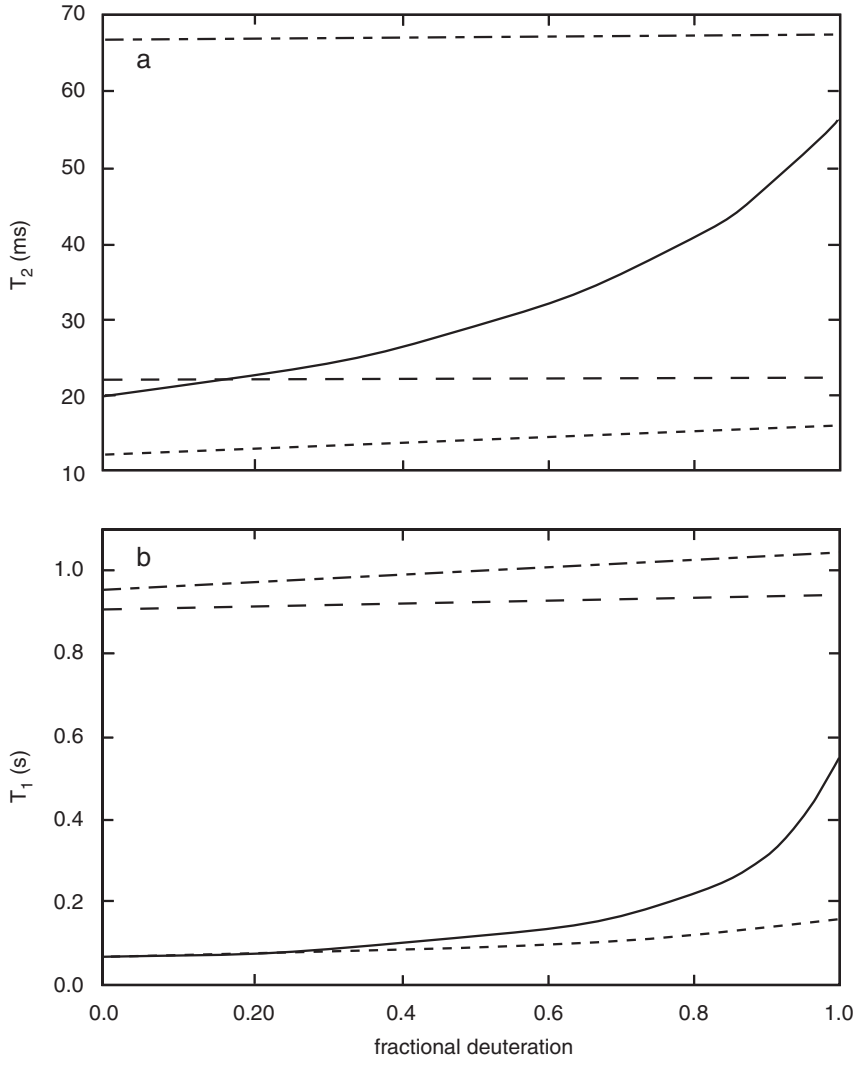

FIGURE 9.2 Calculated average (a) transverse and (b) longitudinal relaxation times as a function of deuteration level, for (—) $^{1}H^{N}$, (- - - -) $^{1}H^{\alpha}$, (– – –) ^{15}N, and (– – –) $^{13}C^{\alpha}$ nuclei in a protein with a correlation time $\tau_c = 12$ ns at a static field strength of 14.1 T. Complete protonation of amide moieties is assumed. Calculations for $^{13}C^{\alpha}$ assume that the heteronucleus of interest is protonated. An increase is observed in the transverse and longitudinal relaxation times of all nuclei as the level of deuteration increases; however, the increase is much more pronounced for $^{1}H^{N}$ in both cases.

that include both appropriate scalar coupling and transverse relaxation contributions, to be (*17*)

$$S_r(\mathrm{D/H}) = S_{r\mathrm{H}}(\mathrm{D/H})\, S_{r\mathrm{N}}(\mathrm{D/H}), \qquad [9.1]$$

in which

$$\begin{aligned} S_{r\mathrm{H}}(\mathrm{D/H}) = {} & \exp[(2\tau^{\mathrm{H}} + 2\delta_2)R_{2\mathrm{H}}^{\mathrm{H}} - (2\tau^{\mathrm{D}} + 2\delta_2)R_{2\mathrm{H}}^{\mathrm{D}}] \\ & \times \left\{ \frac{\exp[-2\tau^{\mathrm{D}}(R_{2\mathrm{MQ}}^{\mathrm{D}} + R_{2\mathrm{H}}^{\mathrm{D}})] + \exp[-2\tau^{\mathrm{D}}(R_{2\mathrm{H}}^{\mathrm{D}} + R_{1\mathrm{H}}^{\mathrm{D}})]}{\exp[-2\tau^{\mathrm{H}}(R_{2\mathrm{MQ}}^{\mathrm{H}} + R_{2\mathrm{H}}^{\mathrm{H}})] + \exp[-2\tau^{\mathrm{H}}(R_{2\mathrm{H}}^{\mathrm{H}} + R_{1\mathrm{H}}^{\mathrm{H}})]} \right\} \\ & \times \sin^2(2\pi J_{\mathrm{NH}}\tau^{\mathrm{D}})/\{\sin^2(2\pi J_{\mathrm{NH}}\tau^{\mathrm{H}})\cos^2(2\pi J_{\mathrm{H^N H^\alpha}}\tau^{\mathrm{H}})\}, \end{aligned} \qquad [9.2]$$

$$S_{r\mathrm{N}}(\mathrm{D/H}) = \exp[2\delta_1(\overline{R}_{2\mathrm{N}}^{\mathrm{D}} - \overline{R}_{2\mathrm{N}}^{\mathrm{H}})] \left\{ \frac{\overline{R}_{2\mathrm{N}}^{\mathrm{H}}(1 - \exp[-t_{1\max}\overline{R}_{2\mathrm{N}}^{\mathrm{D}}])}{\overline{R}_{2\mathrm{N}}^{\mathrm{D}}(1 - \exp[-t_{1\max}\overline{R}_{2\mathrm{N}}^{\mathrm{H}}])} \right\}, \qquad [9.3]$$

$$\tau^{\mathrm{X}} = (\pi J_{\mathrm{NH}})^{-1} \tan^{-1}(\pi J_{\mathrm{NH}}/R_{2\mathrm{H}}^{\mathrm{X}}), \qquad [9.4]$$

$$\overline{R}_{2\mathrm{N}}^{\mathrm{X}} = (R_{2\mathrm{N}}^{\mathrm{X}} + R_{2\mathrm{NH}}^{\mathrm{X}})/2, \qquad [9.5]$$

where $\mathrm{X} = \{\mathrm{D},\ \mathrm{H}\}$; $R_{2\mathrm{H}}^{\mathrm{X}}$, $R_{2\mathrm{N}}^{\mathrm{X}}$, $R_{2\mathrm{NH}}^{\mathrm{X}}$, and $R_{2\mathrm{MQ}}^{\mathrm{X}}$ are the transverse relaxation rate constants for in-phase $^1\mathrm{H}^{\mathrm{N}}$ magnetization, in-phase $^{15}\mathrm{N}$ magnetization, antiphase $^{15}\mathrm{N}$ magnetization, and $^1\mathrm{H}$–$^{15}\mathrm{N}$ multiple-quantum coherence, respectively, in protonated ($\mathrm{X} = \mathrm{H}$) or deuterated ($\mathrm{X} = \mathrm{D}$) backgrounds; and $R_{1\mathrm{H}}^{\mathrm{X}}$ is the longitudinal relaxation rate constant for $^1\mathrm{H}^{\mathrm{N}}$ magnetization in protonated ($\mathrm{X} = \mathrm{H}$) or deuterated ($\mathrm{X} = \mathrm{D}$) backgrounds. The delay $\tau = \tau^{\mathrm{X}}$ is the optimal INEPT transfer delay adjusted for relaxation, and the delays δ_1 and δ_2 encompass the coherence-selection gradients, as was shown in Fig. 7.12. The expression for $S_r(\mathrm{D/H})$ is approximate because differences in $R_{1\mathrm{H}}^{\mathrm{H}}$ and $R_{1\mathrm{H}}^{\mathrm{D}}$ are neglected during the recycle delay.

Venters and co-workers measured the relative sensitivity for perdeuterated and fully protonated human carbonic anhydrase II (HCA II), a protein of ~29 kDa, $\tau_c = 11.4$ ns at 30°C (*22*). The average gain in sensitivity was a factor of 1.7 for α-helix residues and 2.8 for β-sheet residues. Using values of $t_{1\max} = 51.0$ ms, $\delta_1 = 5.5$ ms, $\delta_2 = 1.2$ ms, $\tau^{\mathrm{D}} = \tau^{\mathrm{H}} = 2.5$ ms, $J_{\mathrm{NH}} = 92$ Hz, and $J_{\mathrm{H^N H^\alpha}} = 4.5$ Hz for an α-helix and 9.0 Hz for a β-sheet in [9.1] yields a theoretical gain in the signal-to-noise ratio in the gradient-enhanced, sensitivity-enhanced $^1\mathrm{H}$–$^{15}\mathrm{N}$ HSQC

experiment of 1.4 for residues in α-helices and 3.0 for residues in β-sheets. These theoretical results are in good agreement with the experimental measurements.

9.1.4 ^{2}H ISOTOPE SHIFTS

Replacing a hydrogen atom with a deuteron causes isotope effects on the chemical shifts of nuclei within as many as four covalent bonds of the site of substitution (*38–40*). As a result, ^{13}C chemical shifts in a fully protonated protein, $\delta_{C(H)}$, will be different than those in a perdeuterated protein, $\delta_{C(D)}$ (*17, 22, 35, 40, 41*). To convert $\delta_{C(H)}$ to $\delta_{C(D)}$, or *vice versa*, the ^{2}H isotope effect, $\Delta C(^2H)$ must be calculated for each carbon atom in a perdeuterated protein.

Venters et al. have measured $\Delta C^{\alpha}(^2H)$ and $\Delta C^{\beta}(^2H)$ for all residue types by comparing the ^{13}C chemical shifts in perdeuterated and protonated HCA II (*17, 22*). A statistical analysis suggests that ^{2}H isotope effects can be predicted for $^{13}C^{\alpha}$ and $^{13}C^{\beta}$ chemical shifts in perdeuterated proteins, as shown in Table 9.1. The values in Table 9.1 are consistent with average values of $^1\Delta C(^2H) = -0.25$ and $^2\Delta C(^2H) = -0.1$ ppm measured by Gardner and co-workers (*41*).

Isotope effects are cumulative, and so, for ^{13}C nuclei at positions surrounded by many deuterons, such as those in the middle of long amino acid side chains, total isotope shifts of over 1 ppm can be expected. For backbone nuclei, isotope shifts on the order of -0.3 ppm

TABLE 9.1
Total Deuterium Isotope Shifts for $^{13}C^{\alpha}$ and $^{13}C^{\beta}$ Nuclei[a]

Residue	ΔC^{α} (ppm)	ΔC^{β} (ppm)
Asn, Asp, Ser, His, Phe, Trp, Tyr, Cys	−0.55	−0.71
Lys, Arg, Pro	−0.69	−1.11
Gln, Glu, Met	−0.69	−0.97
Ala	−0.68	−1.00
Ile	−0.77	−1.28
Leu	−0.62	−1.26
Thr	−0.63	−0.81
Val	−0.84	−1.20

[a] $^1\Delta C(^2H)$ (one bond) $= -0.29 \pm 0.05$ ppm; $^2\Delta C(^2H)$ (two bond) $= -0.13 \pm 0.02$ ppm; $^3\Delta C(^2H)$ (three bond) $= -0.07 \pm 0.02$ ppm; $^1\Delta C_{gly}(^2H) = -0.39 \pm 0.04$ ppm (measured separately).

for ^{15}N and -0.5 ppm for $^{13}C^{\alpha}$ for highly deuterated proteins are typical. In addition, the $^{13}C^{\alpha}$ deuterium isotope shifts appear to be weakly dependent on secondary structure (*42*). These predictable properties allow the dependable transfer of ^{13}C chemical shift assignments from perdeuterated to protonated molecules. Thus, estimated ^{13}C side chain isotope shifts can be used to assign $^{13}C/^{15}N$- and $^{13}C/^{13}C$-separated NOESY spectra recorded on protonated protein samples. In addition, the corrected $^{13}C^{\alpha}$ (H) and $^{13}C^{\beta}$ (H) chemical shifts can be used to accurately discern α-helical and β-strand components of secondary structure (*43, 44*).

Perdeuteration ensures a homogeneous ^{2}H isotopic environment for ^{13}C and ^{15}N nuclei and guarantees that losses in both sensitivity and resolution arising from the multibond ^{2}H isotope effect are minimized (*3, 22, 38*). In contrast, random fractional deuteration of uniformly ^{13}C-labeled proteins gives rise to all possible CH_nD_m *isotopomers* for each aliphatic carbon moiety. The ^{13}C chemical shift of a particular aliphatic carbon depends not only on its isotopomeric state (n and m values), but also on the isotopomeric state of aliphatic carbon groups both one and two bonds removed. Because of this multibond ^{2}H isotope effect, random fractional deuteration produces a distribution of ^{13}C chemical shifts for aliphatic carbons, especially methylene and methyl groups, thereby decreasing both sensitivity and resolution in heteronuclear NMR experiments.

The ^{13}C broadening induced by ^{2}H isotope effects is more evident for experiments recorded with high resolution in the ^{13}C indirect dimension of multidimensional NMR spectra. This point is somewhat ironic. Deuteration increases ^{13}C T_2 so that higher resolution data can be collected, but random fractional deuteration introduces ^{2}H isotopomeric resonance shifts that adversely affect resolution. This problem can be addressed, to some degree, by employing 4D rather than 3D heteronuclear experiments. As a rule, 4D ^{13}C experiments are recorded with a small number of increments in ^{13}C indirect dimensions. Consequently, any ^{2}H isotope effects that are smaller than the limited digital resolution of the 4D spectrum will not be as apparent (*17, 22*).

9.1.5 EXPERIMENTS FOR $^{1}H^{N}$, ^{15}N, $^{13}C^{\alpha}$, $^{13}C^{\beta}$, AND ^{13}CO ASSIGNMENTS IN DEUTERATED PROTEINS

Generally, only minor modifications need to be made to the conventional 3D and 4D heteronuclear pulse sequences discussed in Chapter 7 for use on deuterated proteins. The most important change

is that composite pulse deuterium decoupling must be applied whenever transverse ^{13}C magnetization is present, so that evolution of the scalar coupling interaction between the deuteron and its attached carbon is eliminated and scalar relaxation of the second kind, due to short ^{2}H T_1 relaxation times, is minimized (*18*).

Longer ^{13}C T_2 relaxation times allow incorporation of pulse sequence elements that would normally result in excessive sensitivity losses for protonated protein samples. In particular, constant-time evolution periods on the order of $1/^{1}J_{CC}$ (~25–30 ms) can be used to remove passive homonuclear scalar coupling interactions when indirectly recording carbon chemical shifts (Sections 7.1.1.4 and 7.1.3.1). The resulting line narrowing increases both resolution and sensitivity and has been discussed in Section 7.1.3.1.

Substitution of deuterons increases the T_1 values of the remaining ^{1}H spins ($^{1}H^{N}$ in the case of perdeuteration), with this effect particularly evident for perdeuterated proteins. Because a majority of experiments for generating backbone assignments in deuterated proteins begin with magnetization originating on $^{1}H^{N}$ spins, increases in $^{1}H^{N}$ T_1 values are detrimental to overall sensitivity. Estimating H^{N} T_1 values by 1D inversion recovery methods (Section 3.8.2.5) is recommended so that appropriate relaxation delays can be employed between successive scans (Section 3.6.2.5). Techniques for optimizing recovery of magnetization between transients have been discussed (*45–47*).

A number of experiments are available for obtaining the assignments of $^{1}H^{N}$, ^{15}N, $^{13}C^{\alpha}$, $^{13}C^{\beta}$, and ^{13}CO resonances in deuterated proteins (*2, 13, 18, 20, 25, 35, 37, 48*). Rather than review all available or popular pulse sequences for the study of deuterated proteins, the following discussion focuses on illustrative examples in order to highlight the most salient features of pulse sequence design for use with deuterated proteins.

A particularly useful suite of triple-resonance experiments includes the CT-HNCA, CT-HN(CO)CA, HN(CA)CB, and HN(COCA)CB, (*13, 49*). The magnetization transfer pathways for these experiments are, respectively,

$$^{1}H_i^{N} \xrightarrow{J_{NH}} {}^{15}N_i \xrightarrow{{}^{1}J_{NC^{\alpha}}/{}^{2}J_{NC^{\alpha}}} {}^{13}C_i^{\alpha}(t_1)/{}^{13}C_{i-1}^{\alpha}(t_1) \xrightarrow{{}^{1}J_{NC^{\alpha}}/{}^{2}J_{NC^{\alpha}}} {}^{15}N_i(t_2) \xrightarrow{J_{NH}} {}^{1}H_i^{N}(t_3), \quad [9.6]$$

$$^{1}H_i^{N} \xrightarrow{J_{NH}} {}^{15}N_i \xrightarrow{J_{NCO}} {}^{13}CO_{i-1} \xrightarrow{J_{C^{\alpha}CO}} {}^{13}C_{i-1}^{\alpha}(t_1) \xrightarrow{J_{C^{\alpha}CO}} {}^{13}CO_{i-1} \xrightarrow{J_{NCO}} {}^{15}N_i(t_2) \xrightarrow{J_{NH}} {}^{1}H_i^{N}(t_3), \quad [9.7]$$

$$^1H_i^N \xrightarrow{J_{NH}} {}^{15}N_i \xrightarrow{{}^1J_{NC^\alpha}/{}^2J_{NC^\alpha}} {}^{13}C_i^\alpha/{}^{13}C_{i-1}^\alpha \xrightarrow{J_{CC}} {}^{13}C_i^\beta/{}^{13}C_{i-1}^\beta(t_1)$$
$$\xrightarrow{J_{CC}} {}^{13}C_i^\alpha/{}^{13}C_{i-1}^\alpha \xrightarrow{{}^1J_{NC^\alpha}/{}^2J_{NC^\alpha}} {}^{15}N_i(t_2) \xrightarrow{J_{NH}} {}^1H_i^N(t_3), \qquad [9.8]$$

$$^1H_i^N \xrightarrow{J_{NH}} {}^{15}N_i \xrightarrow{J_{NCO}} {}^{13}CO_{i-1} \xrightarrow{J_{C^\alpha CO}} {}^{13}C_{i-1}^\alpha \xrightarrow{J_{CC}} {}^{13}C_{i-1}^\beta(t_1)$$
$$\xrightarrow{J_{CC}} {}^{13}C_{i-1}^\alpha \xrightarrow{J_{C^\alpha CO}} {}^{13}CO_{i-1} \xrightarrow{J_{NCO}} {}^{15}N_i(t_2) \xrightarrow{J_{NH}} {}^1H_i^N(t_3). \qquad [9.9]$$

The magnetization transfer pathways for these pulse sequences are essentially the same as for the equivalent sequences used for protonated protein. Full product operator analyses for these experiments are provided in Sections 7.4.1, 7.4.2, and 7.4.5.3. The experimental pulse sequences presented here use water flip-back solvent suppression techniques and PEP gradient- and sensitivity-enhanced HSQC reverse polarization schemes for obtaining $^1H^N$–^{15}N correlations. As for other triple-resonance experiments (Section 7.4.1.5), the HSQC pulse sequence elements can be replaced by TROSY sequences (Section 7.1.3.3) for increased sensitivity and resolution for larger proteins at high static magnetic field strengths.

9.1.5.1 Constant-Time HNCA for Deuterated Proteins Figure 9.3 shows a constant-time (CT) HNCA pulse scheme for correlating $^1H^N$ and ^{15}N nuclei with both inter- and intraresidue $^{13}C^\alpha$ nuclei in deuterated proteins. This experiment is very similar to the pulse sequence shown in Fig. 7.31d and only important differences are discussed.

The $^{13}C^\alpha$ shift evolution (t_1) occurs during the constant-time period $2T_C \sim 1/{}^1J_{CC}$, thereby eliminating the effects of one-bond ^{13}C–^{13}C scalar couplings. During the constant-time period, when transverse ^{13}C operators are present, ^2H decoupling is employed. The ^1H decoupling during $2T_C$ is not needed for perdeuterated proteins, but may be required, depending on molecular size, for random fractionally deuterated proteins. For large proteins, ^1H decoupling can be omitted, even for fractionally deuterated samples, because signals from the ^1H-bound ^{13}C spins will decay rapidly during the $2T_C$ period. Decoupling sequences must be interrupted when gradients are applied. The 90° pulses flanking the ^1H decoupling periods ensure that the water magnetization is along the z-axis during application of gradient pulses, but is spin-locked during decoupling. The 90° pulses flanking the deuterium decoupling periods ensure that the deuterium magnetization is spin-locked during decoupling to minimize disturbance of the ^2H lock signal.

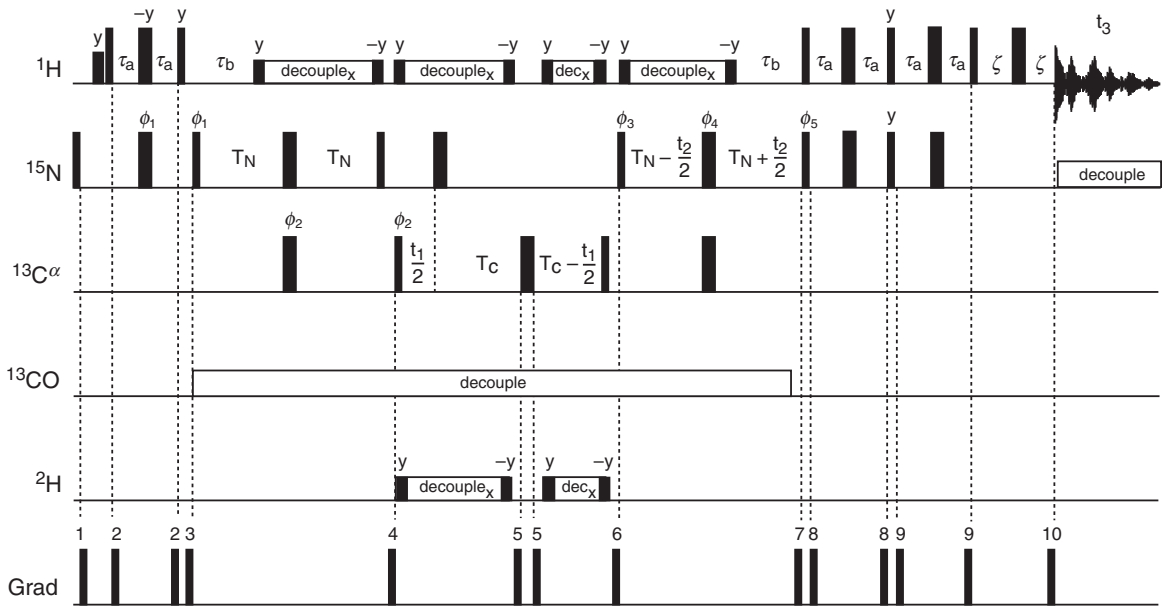

FIGURE 9.3 Pulse sequence for a 3D constant-time HNCA experiment for use on deuterated proteins. Thin and thick bars represent 90° and 180° pulses, respectively. Pulses are applied along the x-axis unless noted. The ^{1}H pulse shown as a short wide bar is a soft 90° selective-water pulse. Pulses bracketing the ^{1}H and ^{2}H decoupling periods are at the same field strength as the decoupling sequence. Decoupling sequences are turned off during gradient pulses. Delays are $2\tau_a = \tau_b \sim 1/(2J_{NH})$, $2T_N \sim 22$–28 ms; $2T_c \sim 1/^{1}J_{CC}$; and ζ is long enough to accommodate the enclosed gradient. The phase cycle is $\phi_1 = x, -x$; $\phi_2 = 2(x), 2(-x)$; $\phi_3 = x$; $\phi_4 = 4(x), 4(-x)$; $\phi_5 = x$; and receiver $= x, -x, -x, x$. Gradients 7 and 10 are used to select the appropriate ^{15}N coherence transfer pathway. Quadrature detection in the F_1 dimension is performed using the TPPI–States method applied to ϕ_2 and the receiver. Frequency discrimination in the F_2 dimension and sensitivity enhancement is achieved as described in Section 7.1.3.2. For each t_2 increment, N- and P-type coherences are obtained by recording two data sets. Gradient 7 and the phase ϕ_5 are inverted in the second data set. For each t_2 increment, ϕ_3 is incremented by 180° in concert with the receiver.

This general pulse scheme can be used for studying both perdeuterated and random fractionally deuterated proteins (taking into account the comments concerning ^{1}H decoupling). A CT-HN(CO)CA experiment, providing solely interresidue connections between $^1H_i^N$, $^{15}N_i$, and $^{13}C_{i-1}^{\alpha}$ spins, is recorded to complement the CT-HNCA.

9.1.5.2 HN(CA)CB for Deuterated Proteins The chemical shifts of the $^{13}C^{\beta}$ spins are assigned using HNCACB experiments (Section 7.4.5.3). Figure 9.4 shows a general pulse sequence for recording HNCACB-type data on deuterated proteins and is similar to Fig. 7.47.

The product operator analysis in Section 7.4.5.3 shows that the intensities of $^{13}C^{\alpha}$ correlation peaks are proportional to $\cos^2(2\pi {}^1J_{CC}T_C)$ and the intensities of $^{13}C^{\beta}$ correlation peaks are proportional to $\sin^2(2\pi {}^1J_{CC}T_C)$. In the conventional HNCACB experiment (Section 7.4.5.3), the delay T_C is normally set to $\sim 1/(8\,{}^1J_{CC})$, so that both $^{13}C^{\alpha}$ and $^{13}C^{\beta}$ peaks are obtained with approximately equal intensities; however, each set of peaks has only one-half of the maximum possible intensity. In principle, optimal transfer to the $^{13}C^{\beta}$ spins can be achieved by setting $T_C \sim 1/(4\,{}^1J_{CC})$. In this case, $^{13}C^{\alpha}$ transverse magnetization is present for $4T_C \sim 1/{}^1J_{CC} \sim$ 28 ms. In fully protonated larger proteins, this approach is impractical because efficient $^{13}C^{\alpha}$ relaxation losses during these delays degrade sensitivity. In deuterated samples, the $^{13}C^{\alpha}$ T_2 is significantly longer and a value of $4T_C \sim 1/{}^1J_{CC}$ can be used to transfer all magnetization to the $^{13}C^{\beta}$ spins, thereby increasing sensitivity for these correlations. For this reason, the experiment is referred to as an HN(CA)CB experiment (*13*). The pulse sequence shown in Fig. 9.4 is appropriate for random fractionally deuterated proteins. For perdeuterated proteins, ^{1}H decoupling does not need to be applied between the first and last 90° pulses on ^{13}C spins.

The HN(CA)CB sequence shown in Fig. 9.4 uses conventional incrementation for the t_1 evolution period, rather than a constant-time evolution t_1 period. Experiments that measure $^{13}C^{\beta}$ chemical shifts using constant-time periods on the order of $1/{}^1J_{CC}$ suffer from sensitivity losses, compared to non-constant-time experiments, unless both $^{13}C^{\alpha}$ and $^{13}C^{\beta}$ nuclei involved in the coherence transfer process are perdeuterated (*13*). The fraction of $^{13}C^{\alpha}$ and $^{13}C^{\beta}$ spin pairs that are perdeuterated decreases rapidly as the level of fractional deuteration is reduced. For example, if a protein is randomly deuterated to a fraction f, without any biased deuteration patterns resulting from biosynthetic pathways, then the fraction of perdeuterated $^{13}C^{\alpha}D$–$^{13}C^{\beta}D_2$ moieties is f^3 for an amino acid residue with a β-methylene group. Consequently, non-constant-time versions of the HN(CA)CB [and the complementary

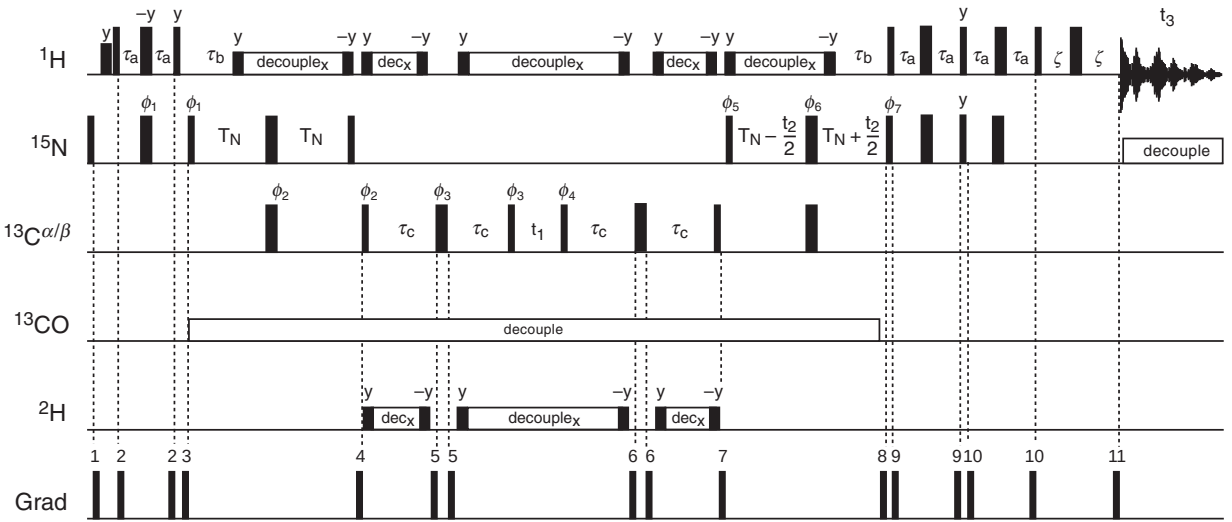

FIGURE 9.4 Pulse sequence for a 3D HN(CA)CB experiment for use on deuterated proteins. Thin and thick bars represent 90° and 180° pulses, respectively. Pulses are applied along the x-axis unless noted. The short wide rectangle is an ^{1}H selective 90° water pulse. Pulses bracketing the ^{1}H decoupling periods are at the same field strength as the decoupling sequence. These pulses ensure that the water magnetization is along the z-axis during application of gradient pulses, but is spin-locked during decoupling. Decoupling sequences are turned off during gradient pulses. Delays are discussed in the text, but the small delay ζ is to accommodate gradients. The phase cycle is $\phi_1 = x, -x$; $\phi_2 = 2(x), 2(-x)$; $\phi_3 = 4(y), 4(-y)$; $\phi_4 = 8(y), 8(-y)$; $\phi_5 = x$; $\phi_6 = 4(x), 4(-x)$; $\phi_7 = x$; receiver $= x, -x, -x, x$. Gradients 8 and 11 are used to select the appropriate ^{15}N coherence transfer pathway. Quadrature detection in the F_1 dimension is performed using the TPPI–States method applied to ϕ_2, ϕ_3, and the receiver. Frequency discrimination in the F_2 dimension and sensitivity enhancement is achieved as described in Section 7.1.3.2. For each t_2 increment, N- and P-type coherences are obtained by recording two data sets. Gradient 8 and the phase ϕ_7 are inverted in the second data set. For each t_2 increment, ϕ_5 is incremented by 180° in concert with the receiver.

HN(COCA)CB experiment] are recommended for random fractionally deuterated proteins (*13*). Constant-time versions of the HN(CA)CB and HN(COCA)CB experiments can be used for perdeuterated proteins, as described for the CT-HNCA experiment in Section 9.1.5.1.

9.1.5.3 Other Experiments for Resonance Assignments For determining ^{13}CO assignments, straightforward HNCO experiments, correlating $^{13}CO_{i-1}$, $^{15}N_i$, and $^{1}H_i^N$ spins, and HN(CA)CO experiments, correlating $^{13}CO_i$, $^{15}N_i$, and $^{1}H_i^N$ spins, are performed as described in Sections 7.4.4.1 and 7.4.4.2. The 3D/4D HN(COCA)NH spectrum allows the direct connection of adjacent amide groups along the protein backbone and has the advantage that the spectra are extremely easy to interpret (*18, 50–52*). This experiment utilizes the coherence transfer pathway,

$$\begin{aligned} {}^{1}H_i^N(t_1) &\xrightarrow{J_{NH}} {}^{15}N_i(t_2) \xrightarrow{J_{NCO}} {}^{13}CO_{i-1} \xrightarrow{J_{C^\alpha CO}} {}^{13}C_{i-1}^{\alpha} \\ &\xrightarrow{J_{NC^\alpha}} {}^{15}N_{i-1}(t_3) \xrightarrow{J_{NH}} {}^{1}H_{i-1}^N(t_4), \end{aligned} \qquad [9.10]$$

to generate sequential correlations between the $^{1}H_i^N$, $^{15}N_i$, $^{1}H_{i-1}^N$, and $^{15}N_{i-1}$ backbone atoms. The utility of this experiment, for fully protonated proteins, has been limited predominantly by the large $^{13}C^\alpha$ relaxation rates arising from dipolar coupling between the $^{13}C^\alpha$ and $^{1}H^\alpha$ spins. A significant improvement in sensitivity is realized for perdeuterated proteins because the $^{13}C^\alpha$ T_2 relaxation times are notably increased. Deuterium decoupling should be applied in the HN(CA)CO and HN(COCA)NH experiments when transverse $^{13}C^\alpha$ magnetization is present.

A complementary set of experiments that begin with $^{1}H^\alpha/^{1}H^\beta$ spins has been proposed and therefore these experiments are not useful for application to perdeuterated proteins (*25*). These 4D HBHACBCANH and HBHACBCA(CO)NH experiments provide correlations between $^{1}H^\alpha/^{1}H^\beta$ spins and intra- and interresidue amide moieties in random fractionally deuterated systems. The experiments are adversely affected by ^{13}C isotopomeric broadening, although this effect can be alleviated to some extent by reducing the digital resolution in the ^{13}C dimensions of 4D experiments.

To ensure the highest sensitivity, experiments on deuterated proteins should be performed at the highest possible static magnetic field strength. However, transverse relaxation rates of ^{13}CO spins increase approximately with the square of the static magnetic field strength due to the CSA relaxation mechanism. As a result, the sensitivity of

NMR experiments that transfer magnetization to ^{13}CO spins begins to decrease as the static field increases (for either protonated or deuterated proteins). For example, the usual approach uses the pair of HNCA and HN(CO)CA spectra to obtain sequential assignments; however, the HNCA experiment can be recorded at the largest available field (900 MHz), but the HN(CO)CA experiment usually is recorded at a static magnetic field strength of 14.1 T (600 MHz).

Several HNCA-based approaches that minimize or completely avoid the time during which transverse ^{13}CO magnetization is present have been proposed. Using HNCA methods to obtain sequential connectivities has the inherent problem that the coupling constants $^{1}J_{NC^{\alpha}}$ and $^{2}J_{NC^{\alpha}}$ are similar in size. Consequently, both intra- and interresidue correlations may be observed and can be difficult to differentiate. In one method to circumvent this difficulty, spin state selection is used to distinguish between the intra- and interresidue connectivities (*53*). A second method suppresses the coherence transfer pathway that uses the $^{1}J_{NC^{\alpha}}$ scalar coupling interaction (*54*). A different approach uses a combination of intraresidue and double-quantum (DQ) HNCA experiments (*55*). The intraresidue HNCA experiment correlates the $^{1}H_{i}^{N}$and $^{15}N_{i}$ spins exclusively with the $^{13}C_{i}^{\alpha}$ spin. The DQ HNCA experiment correlates the $^{1}H_{i}^{N}$and $^{15}N_{i}$ spins with the sum of the frequencies of the $^{13}C_{i}^{\alpha}$ and$^{13}C_{i-1}^{\alpha}$. The sequential correlation between $^{1}H_{i}^{N}$ and $^{13}C_{i-1}^{\alpha}$ spins is established by subtraction of the matching $^{13}C_{i}^{\alpha}$ shift from the DQ resonance frequency.

The preceding sections have discussed general methods, and caveats, for obtaining backbone $^{1}H^{N}$, ^{15}N, $^{13}C^{\alpha}$, and $^{13}C^{\beta}$ assignments in larger proteins (>20 - 30 kDa). Perdeuteration, rather than random fractional deuteration, of proteins is warranted to obtain maximum sensitivity in out-and-back experiments originating and terminating on the $^{1}H^{N}$ spins, particularly for experiments that utilize transfer between multiple aliphatic ^{13}C spins.

9.1.6 SIDE CHAIN ^{13}C ASSIGNMENTS IN DEUTERATED PROTEINS

Correlations to ^{13}C spins further down the amino acid side chain than C^{β} can be made by inserting additional magnetization transfer steps into the HN(CA)CB experiment. For example, addition of a pair of ^{13}C–^{13}C pulse-interrupted free-precession (COSY-type) steps before and after t_1 (τ_c–180–τ_c in Fig. 9.4) produces an HN(CACB)CG experiment that correlates the $^{13}C^{\gamma}$ spin to the amide moiety (*22, 33*). The sequence can be extended in similar fashion to obtain correlations to C^{δ} and even C^{ε} positions in the side chain. These HN(CX)$_n$CY experiments also

are useful for editing the spectra of particular amino acids based on the branch point of the side chain. For example, Ile and Leu have similar $^{13}C^{\beta}$ chemical shifts, but branch at different locations (Ile at C^{β}, Leu at C^{γ}). As a result, Leu residues give stronger correlations than do Ile residues in an HN(CACB)CG experiment (*17*). However, each additional COSY-style pulse element requires a delay of length of $\sim 1/(2J_{CC})$, resulting in reduced sensitivity for experiments that correlate spins farther along the side chain.

For moderately sized $^{13}C/^{15}N$ labeled proteins, side chain ^{13}C assignments are most commonly obtained from the HCCH–TOCSY (Section 7.4.4.2) experiment or the (H)CC(CO)NH–TOCSY experiment (*56*). These experiments also can be used with random fractionally deuterated proteins to obtain side chain ^{13}C assignments; however, rapid relaxation of the residual proton-bound ^{13}C spins reduces sensitivity and restricts the usefulness of these experiments. For example, if a protein is randomly deuterated to a fraction f, without any biased deuteration patterns resulting from biosynthetic pathways, then the fraction of $^{13}C^{\alpha}D$–$^{13}C^{\beta}D_2$–$^{13}C^{\gamma}HD$ moieties is $(1-f)f^4$ for an amino acid residue with β- and γ-methylene groups. Consequently, the probability is high that the ^{13}C–^{13}C TOCSY transfer will pass magnetization through a protonated $^{13}C^{\alpha}$ or $^{13}C^{\beta}$ site, quickly reducing the sensitivity of the experiment for correlations to the $^{13}C^{\gamma}$ spin and to spins farther along the side chain. Protein samples prepared using higher levels of deuteration or perdeuteration cannot be used to overcome this disadvantage because HCCH–TOCSY and (H)CC(CO)NH–TOCSY experiments begin from magnetization of a carbon-attached ^{1}H spin.

The CC(CO)NH–TOCSY experiment is a modification of the (H)CC(CO)NH–TOCSY that begins from ^{13}C, rather than ^{1}H, magnetization (*57*). The concomitant fourfold reduction in sensitivity, due to the smaller magnetogyric ratio of ^{13}C, is compensated by the increase in ^{13}C T_2 at each position in the side chain (*57*). In theory, sensitivity gains as large as a factor of seven are obtained from the reduced relaxation losses for methylene groups in perdeuterated, compared to fully protonated, proteins (*22, 58–60*). However, the ^{13}C T_1 is longer by approximately a factor of two in perdeuterated proteins (Fig. 9.2); therefore, longer recycle delays are necessary, which reduces the overall signal-to-noise ratio per unit time.

The pulse sequence for the CC(CO)NH–TOCSY experiment is shown in Fig. 9.5. This experiment utilizes the coherence transfer pathway,

$$^{13}C_i(t_1) \xrightarrow{J_{CC}} {}^{13}C_i^{\alpha} \xrightarrow{J_{C^{\alpha}CO}} {}^{13}CO_i \xrightarrow{J_{NCO}} {}^{15}N_{i+1}(t_2) \xrightarrow{J_{NH}} {}^{1}H_{i+1}^{N}(t_3), \qquad [9.11]$$

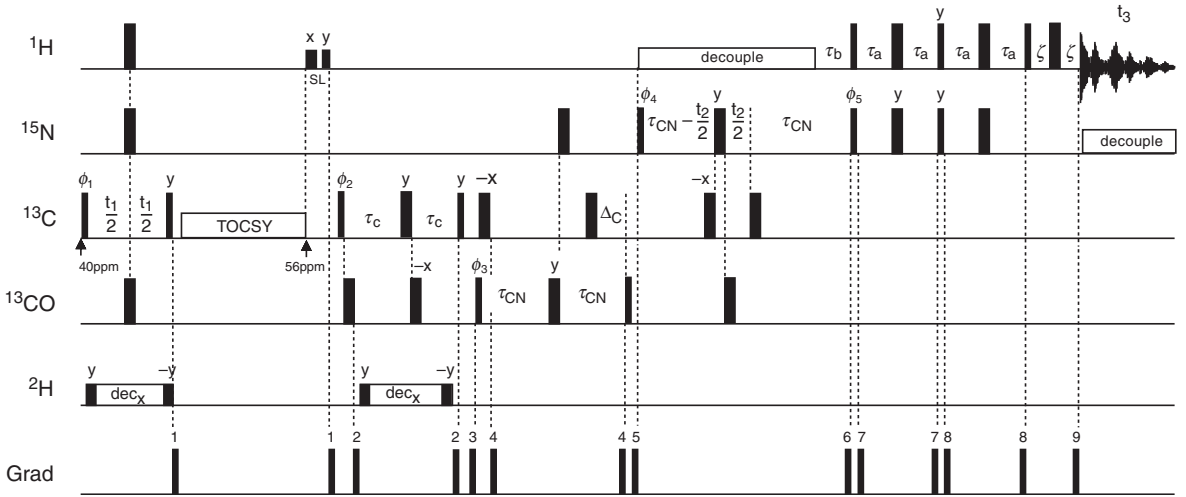

FIGURE 9.5 Pulse sequence for the 3D gradient-enhanced, sensitivity-enhanced CC(CO)NH–TOCSY experiment for use on deuterated proteins. Thin and thick bars represent 90° and 180° pulses, respectively. Pulses labeled SL are spin lock purge pulses. Pulses are applied along the x-axis unless noted. Initially, ^{13}C pulses are broadband and centered at ~40 ppm. Where noted, the ^{13}C transmitter is shifted to ~56 ppm (middle of $^{13}C^{\alpha}$ region) and subsequent pulses are $^{13}C^{\alpha}$ selective. Delays: $\tau_c \sim 1/(4J_{C^{\alpha}CO})$ (slightly less to account for relaxation); $\tau_{CN} = 1/(4J_{NCO})$; $\Delta_C = 1/(4J_{C^{\alpha}CO})$; $\tau_a \sim 1/(4J_{NH})$; $\tau_b \sim 1/(2J_{NH})$; and ζ long enough to accommodate gradients. The phase cycle is $\phi_1 = 4(y), 4(-y)$; $\phi_2 = 8(x), 8(-x)$; $\phi_3 = 2(x), 2(-x)$; $\phi_4 = x, -x$; $\phi_5 = x$; receiver $= x, 2(-x), x, -x, 2(x), 2(-x), 2(x), -x, x, 2(-x), x$. Gradients 6 and 9 are used to select the appropriate ^{15}N coherence transfer pathway. Quadrature detection in the F_1 dimension is performed using the TPPI–States method applied to ϕ_1 and the receiver. Frequency discrimination in the F_2 dimension and sensitivity enhancement are achieved as described in Section 7.1.3.2. For each t_2 increment, N- and P-type coherences are obtained by recording two data sets. Gradient 6 and the phase ϕ_5 are inverted in the second data set. For each t_2 increment, ϕ_4 is incremented by 180° in concert with the receiver.

to obtain correlations between the side chain ^{13}C spins of residue i with the amide group of residue $i+1$. The experiment begins by recording side chain ^{13}C chemical shifts during t_1. The evolution period is followed by a z-filtered ^{13}C–^{13}C TOCSY isotropic mixing sequence. The isotropic mixing time is chosen as for the HCCH–TOCSY experiment (Section 7.3.3). The magnetization that is transferred to the $^{13}C^{\alpha}$ spin during the TOCSY period subsequently is transferred in a "straight-through" fashion to the ^{13}CO, ^{15}N, and $^{1}H^{N}$ spins.

Figure 9.6 shows strips taken from a CC(CO)NH–TOCSY spectrum of perdeuterated $^{2}H/^{13}C/^{15}N$ calbindin D_{28k} (~30 kDa). Each strip shows the side chain ^{13}C chemical shifts of several lysine residues correlated with the amide ^{15}N and $^{1}H^{N}$ shifts of the succeeding residue.

9.1.7 SIDE CHAIN ^{1}H ASSIGNMENTS

Two approaches are available for obtaining the assignment of side chain ^{1}H resonances in larger proteins, although neither is ideal. In one approach, $^{13}C(D)$ side chain assignments are obtained from a CC(CO)NH–TOCSY recorded on a perdeuterated protein sample. The $^{13}C(D)$ side chain chemical shifts are used to estimate $^{13}C(H)$ side chain chemical shifts using ^{2}H isotope shift information (Table 9.1). A 4D HCC(CO)NH–TOCSY is recorded on a random fractionally deuterated or fully protonated sample to obtain ^{1}H side chain assignments. In the other approach, $^{13}C(H)$ carbon and ^{1}H proton side chain shifts are obtained directly from a 4D HCC(CO)NH–TOCSY recorded on a random fractionally deuterated or fully protonated sample. The advantage of the second method is that $^{13}C(H)$ shifts do not have to be estimated. However, full assignment of $^{13}C(H)$ carbon side chain shifts might not be achieved because of relaxation losses arising from the short ^{13}C T_2 values. As discussed in Section 9.1.4, line narrowing observed in the spectra of random fractionally deuterated proteins is offset by the isotopomer broadening effect. These effects can be minimized by (*i*) using higher levels of deuteration (e.g., 70%) and/or (*ii*) using 4D experiments with a limited number of points in the carbon dimensions. Overall, applying both approaches may prove fruitful. The limited data that are extracted easily from the 4D HCC(CO)NH–TOCSY experiment recorded on a fully protonated sample can be used to confirm information obtained from the spectra recorded on random fractionally deuterated samples, particularly in corroborating ^{2}H isotope shifts. In studies of ~30-kDa calbindin D_{28k}, ~50% of the side chain ^{1}H assignments were made from a 4D HCC(CO)NH–TOCSY experiment on a fully protonated sample.

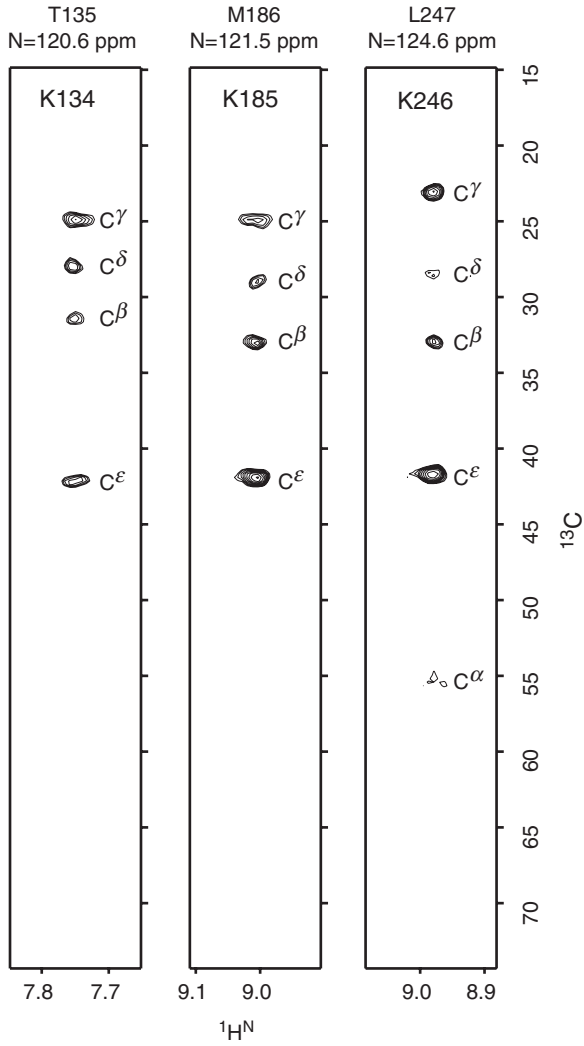

FIGURE 9.6 Strip plots from a 3D CC(CO)NH–TOCSY on perdeuterated $^{2}H/^{13}C/^{15}N$ calbindin D_{28k}. The strips show side chain ^{13}C chemical shifts of selected lysine residues throughout the protein correlated with the $^{1}H^{N}$ and ^{15}N chemical shifts of the $i+1$ residue. The TOCSY mixing time is 20 ms. The spectrum was recorded on a 600-MHz NMR spectrometer.

9.1.8 NOE RESTRAINTS FROM DEUTERATED PROTEINS

^1H–^1H NOEs are the primary data used to generate restraints for protein structure determination by NMR spectroscopy. As discussed previously, sizeable gains in sensitivity are attainable for many triple-resonance scalar correlation experiments by using proteins perdeuterated at nonexchangeable proton sites. Although the use of perdeuterated proteins is optimal for obtaining backbone and side chain ^{13}C assignments, only $^1H^N$–$^1H^N$ NOEs can be obtained from such a sample. Other NOEs must be obtained from fully protonated, random fractionally deuterated, or selectively protonated protein samples.

9.1.8.1 4D H^N–H^N $^{15}N/^{15}N$-Separated NOESY Experiment Perdeuteration decreases both the amide $^1H^N$ R_1 and R_2 relaxation rate constants. Taking advantage of these characteristics, up to a sevenfold increase in signal-to-noise ratio can be realized for a perdeuterated protein relative to its protonated counterpart in a 4D $^1H^N$–$^1H^N$ NOESY experiment (*22, 58–60*). Additionally, perdeuteration significantly reduces spin diffusion effects, allowing the use of notably longer NOE mixing times, up to several hundred milliseconds (*17, 33, 40, 58–60*). As a result of the longer mixing times, NOEs over greater distances (up to 8 Å) potentially can be obtained. However, even in perdeuterated proteins, short distances between amide $^1H^N$ spins in α-helices can result in spin diffusion; recording a series of NOESY spectra for different mixing times can aid in detecting such effects.

A gradient-enhanced, sensitivity-enhanced 4D $^{15}N/^{15}N$-separated NOESY experiment for use on a $^2H/^{13}C/^{15}N$-labeled protein is shown in Fig. 9.7 (*59, 60*). This experiment is very similar to the 3D variant described in Section 7.2.4.1. The overall flow of magnetization is described by

$$\begin{aligned} {}^1H_A^N \xrightarrow{J_{NH}} {}^{15}N_A(t_1) \xrightarrow{J_{NH}} {}^1H_A^N(t_2) \xrightarrow{NOE} {}^1H_B^N \\ \xrightarrow{J_{NH}} {}^{15}N_B(t_3) \xrightarrow{J_{NH}} {}^1H_B^N(t_4). \end{aligned} \qquad [9.12]$$

The frequency axes in the 4D spectrum correspond to $F_1 = \delta(^{15}N_A)$, $F_2 = \delta(^1H_A^N)$, $F_3 = \delta(^{15}N_B)$, $F_4 = \delta(^1H_B^N)$. The resulting 4D spectrum correlates amide group A to a spatially close amide group B, via the NOE. The 4D $^{15}N/^{15}N$-separated NOESY experiment also can be used with random fractionally deuterated proteins. Spin diffusion effects are also reduced compared to fully protonated samples, but are not reduced to the same degree as for perdeuterated proteins.

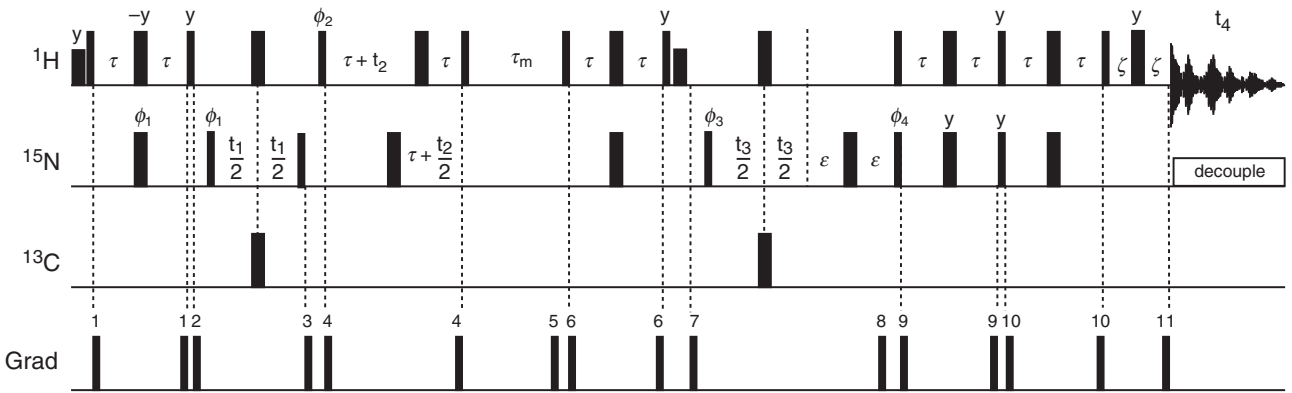

FIGURE 9.7 Pulse sequence of the gradient-enhanced, sensitivity-enhanced 4D ^{15}N/^{15}N-separated NOESY experiment with water flip-back solvent suppression. Deuterium decoupling is not required, because transverse ^{13}C magnetization is never present. Thin and thick bars represent 90° and 180° pulses, respectively. Low-power selective ^{1}H pulses, applied to the H_2O resonance, are shown as short rectangles. Pulses are applied along the x-axis unless noted. The delays are $\tau \sim 1/(4J_{NH})$; τ_m is the NOESY mixing time; ε and ζ are long enough to accommodate the encompassed gradients. The phase cycle is $\phi_1 = x, -x$; $\phi_2 = x$; $\phi_3 = x$; $\phi_4 = x$; receiver $= x, -x$. Gradient 5 is applied at the end of the mixing time to defocus any residual transverse magnetization after radiation damping has returned the H_2O signal to the z-axis. Gradients 8 and 11 are used to select the appropriate ^{15}N coherence transfer pathway. Quadrature detection in the $F_1$and F_2 dimensions is performed using the TPPI–States method applied to ϕ_1 and the receiver, and ϕ_2 and the receiver, respectively. Frequency discrimination in the F_3 dimension and sensitivity enhancement is achieved as described in Section 7.1.3.2. For each t_3 increment, N- and P-type coherences are obtained by recording two data sets. Gradient 8 and the phase ϕ_4 are inverted in the second data set. For each t_3 increment, ϕ_3 is incremented by 180° in concert with the receiver.

The pulse sequence shown in Fig. 9.7 was used to record a 4D H^N–H^N $^{15}N/^{15}N$-separated NOESY spectrum on perdeuterated $^{2}H/^{13}C/^{15}N$ calbindin D_{28k} using a mixing time of 175 ms. Figure 9.8 shows a slice from this 4D $^{15}N/^{15}N$-separated NOESY spectrum. The slice is taken at the $^{15}N/^{1}H^N$ shift(s) of Val62, and the autocorrelation peak of Val62 can be seen in the spectrum at $F_1 = F_3 = 118.2$ ppm (^{15}N) and $F_2 = F_4 = 9.12$ ppm (^{1}H). All other correlations are NOE cross-peaks from the Val62 $^{1}H^N$ spin.

9.1.8.2 $^{13}C/^{15}N$-, $^{13}C/^{13}C$-, and $^{15}N/^{15}N$-Separated NOESY Experiments on Random Fractionally Deuterated Proteins At first sight, random fractionally deuterated proteins appear to be ideal candidates for establishing general ^{1}H–^{1}H NOE contacts using heteronuclear-separated NOESY experiments such as the 3D and 4D

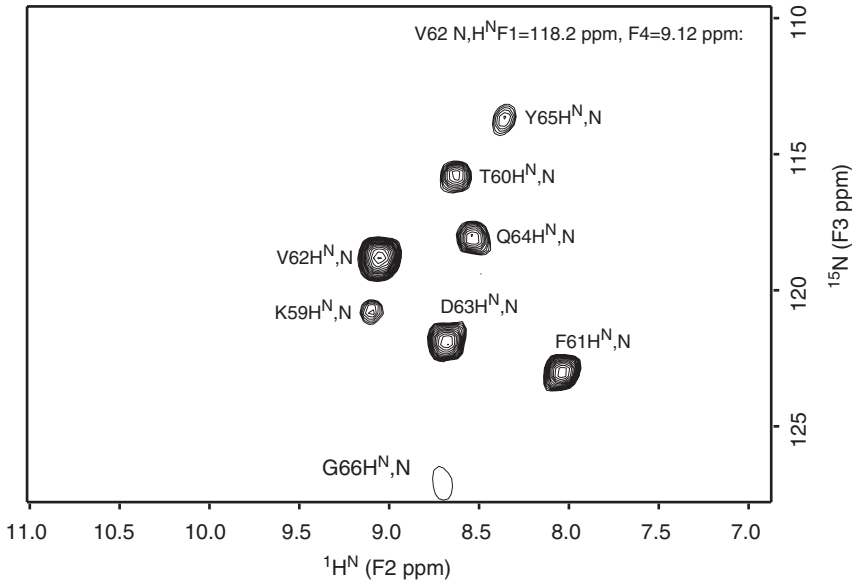

FIGURE 9.8 A 2D slice taken from a 4D $^{15}N/^{15}N$-separated NOESY on perdeuterated calbindin D_{28k}. The data were taken using the pulse sequence described in Fig. 9.7 and a mixing time of 175 ms. The spectrum was recorded on an 800-MHz NMR spectrometer. The slice is taken at the $^{15}N/^{1}H^N$ (F_1/F_4) shift(s) of V62, and the autocorrelation peak of V62 can be seen in the spectrum. Other peaks in the spectrum are NOEs between the amide group of V62 and the indicated amide groups.

$^{13}C/^{15}N$-, $^{13}C/^{13}C$-, and $^{15}N/^{15}N$-separated NOESY experiments discussed in Section 7.2.4 (*25, 58–62*), because, in contrast to perdeuterated molecules, side chain protons are available, albeit at reduced concentrations. However, because the sample is a mixture of different isotopomers, significant variations in relaxation rates may exist between a specific ^1H spin in one protein molecule and the same ^1H spin in a different protein molecule with a different deuterium composition (*63*). These variations pose difficulties for the interpretation of cross-peak intensities in NOESY spectra of random fractionally deuterated proteins.

The relaxation times of ^1H spins increase as proteins are more highly deuterated, which leads to increased intensity of NOE cross-peaks. On the other hand, increasing the level of deuteration dilutes the population of carbon-bound ^1H spins, thereby reducing the intensity of any NOE peak to or from a carbon-bound ^1H spin. Nietlispach, Laue, and co-workers discuss these effects (*25*) and reach the following conclusions. First, the intensities of H^N–H^N NOE peaks rise with increasing level of deuteration. Second, the intensities of H^N–H^α NOE peaks do not drastically change up to a deuteration level of ~50%; at this level the intensities start to decrease. The dilution effect is compensated at low deuteration levels by the favorable relaxation of the remaining ^1H spins, but at higher enrichment levels the dilution effect dominates. Third, NOE peaks between two H^α spins show a decrease in intensity as the level of deuteration increases, because the reduction in ^1H spin population offsets any advantage gained by increases in the relaxation times of the $^1H^\alpha$ spins.

From a practical standpoint, the variation in relaxation rate constants for different molecules in a random fractionally deuterated sample means that NOE cross-peak volumes do not necessarily provide accurate estimates of internuclear distances. Use of average relaxation rate constants calculated by taking population-weighted averages of the rate constants for each isotopomer has been suggested as one approach for treating this problem (*25*). This approach is most useful if the distribution of relaxation rate constants for different isotopomers is narrow, compared to the magnitudes of the relaxation rate constants. A quantitative analysis of cross-relaxation in a random fractionally deuterated system has been discussed (*63*). In this approach, a series expansion is derived that, to second order, expresses cross-peak volume at a specific mixing time independently of autorelaxation or external relaxation effects. In principle, this treatment removes the effect of the degree of deuteration and allows more accurate cross-relaxation rate constants to be established.

In light of these difficulties, random fractionally deuterated proteins have not been widely used for obtaining quantitative ^1H–^1H NOE distance restraints for structure calculations. NOESY data acquired on random fractionally deuterated proteins are perhaps better employed to generate global folds, rather than atomic-resolution structures.

The *n*D-separated NOESY pulse sequences for use with random fractionally deuterated proteins are essentially the same as their counterparts for fully protonated samples (Section 7.2), with the addition of deuterium decoupling when transverse carbon magnetization is present (*25*). A gradient- and sensitivity-enhanced 4D $^{13}C/^{15}N$-separated NOESY experiment is shown in Fig. 9.9. The overall flow of magnetization is

$$\begin{aligned} {}^1H_a &\xrightarrow{J_{CH}} {}^{13}C(t_1) \xrightarrow{J_{CH}} {}^1H_a(t_2) \\ &\xrightarrow{NOE} {}^1H^N \xrightarrow{J_{NH}} {}^{15}N(t_3) \xrightarrow{J_{NH}} {}^1H^N(t_4), \end{aligned} \qquad [9.13]$$

in which ^1H_a is an aliphatic, carbon-attached ^1H spin. This experiment is particularly useful in the study of selectively protonated, otherwise perdeuterated, proteins, as discussed in the following sections.

9.1.9 SELECTIVE PROTONATION

Because the overall success of a structure determination relies on obtaining side chain distance restraints, especially those involving residues in the hydrophobic core of the protein, a "middle-ground" approach for obtaining ^1H–^1H NOEs in larger proteins is available. This technique involves selectively reintroducing ^1H spins into non-exchangeable sites of otherwise perdeuterated proteins. NOESY experiments performed on selectively protonated aliphatic methyl groups (Ile, Leu, Val, Ala) and aromatic side chain rings (Phe, Tyr, Trp) in otherwise perdeuterated proteins provide very useful long-range distance restraints.

To date, the majority of applications of selective protonation has involved methyl ^1H spins, because these spins, although exhibiting somewhat limited chemical shift dispersion, have long T_2 relaxation times, even in ^{13}C-labeled molecules. Kay and co-workers have developed methyl-TROSY techniques, based on the HMQC pulse sequence (Section 7.1.1.1), that provide additional resolution and sensitivity (*64*). Methyl groups also are abundant in the hydrophobic cores of proteins, allowing additional NOE connectivities to be identified and used as restraints for structure calculations.

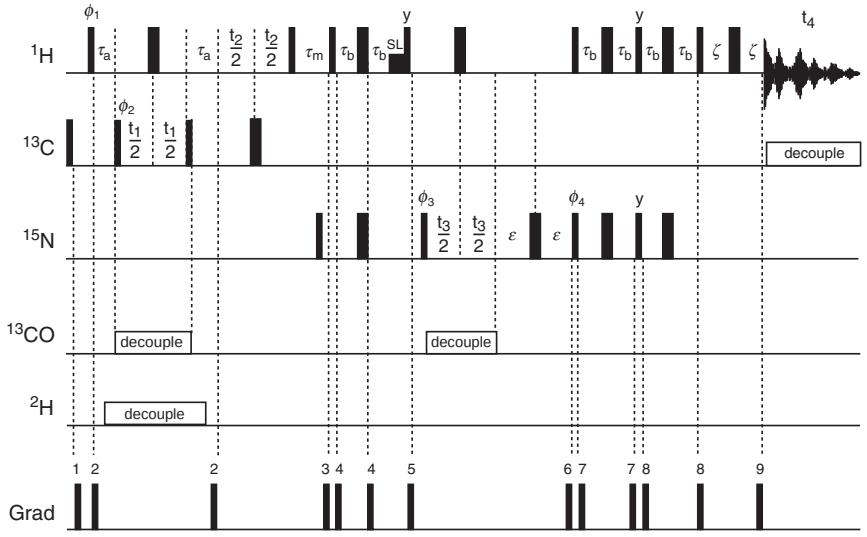

FIGURE 9.9 Pulse sequence of the gradient-enhanced, sensitivity-enhanced 4D $^{13}C/^{15}N$-separated NOESY experiment. Thin and thick bars represent 90° and 180° pulses, respectively. The spin lock pulse applied to the H_2O resonance is denoted SL. Pulses are applied along the x-axis unless noted. The delays are $\tau_a \sim 1/(4J_{CH})$; $\tau_b \sim 1/(4J_{NH})$; τ_m is the NOESY mixing time; ε and ζ are long enough to accommodate the encompassed gradients. The phase cycle is $\phi_1 = 45°$; $\phi_2 = x, -x$; $\phi_3 = x$; $\phi_4 = x$; receiver $= x, -x$. Gradient 3 is applied at the end of the mixing time to defocus any residual transverse magnetization after radiation damping has returned the H_2O signal to the z-axis. Gradients 6 and 9 are used to select the appropriate ^{15}N coherence transfer pathway. Quadrature detection in the $F_1$and F_2 dimensions is performed using the TPPI–States method applied to ϕ_2 and the receiver, and ϕ_1 and the receiver, respectively. Frequency discrimination in the F_3 dimension and sensitivity enhancement are achieved as described in Section 7.1.3.2. For each t_3 increment, N- and P-type coherences are obtained by recording two data sets. Gradient 6 and the phase ϕ_4 are inverted in the second data set. For each t_3 increment, ϕ_3 is incremented by 180° in concert with the receiver.

Rosen et al. developed a protocol using $^1H/^{13}C$ pyruvate as the sole carbon source for biosynthesis of $^2H/^{13}C/^{15}N$ triply labeled proteins with selective protonation at the methyl groups of Ala, Val, Leu and Ile-γ2 (*29*). Goto et al. developed a protocol using [3-^{2}H], ^{13}C α-ketoisovalerate, and ^{13}C α-ketobutyrate to supplement [$^2H/^{13}C$] glucose in bacterial growth media to obtain selective protonation

of Leu-δ, Val-γ, and Ile-δ1 methyl groups; this labeling pattern is abbreviated as ILV (*30, 31*). The level of methyl protonation achieved in these protocols is $>90\%$. Elegant experiments for assigning methyl resonances in methyl-protonated, otherwise perdeuterated, proteins have been developed by Kay and co-workers. Both straight-through and out-and-back experiments are used to correlate the methyl ^{13}C and ^{1}H resonances with previously assigned backbone ^{15}N or ^{13}CO spins (*65*). These samples allow H^N–H^N, H^N–CH_3, and CH_3–CH_3 NOEs to be measured using 4D ^{15}N, ^{15}N-edited NOESY; 4D ^{13}C, ^{15}N-edited NOESY; and ^{13}C, ^{13}C-edited NOESY experiments, respectively (*25, 58–62*). The limited number of ^{1}H spins in the protein again means that spin diffusion effects are minimized, allowing the use of longer NOE mixing times in these experiments.

Figure 9.10 shows slices from 3D ^{13}C, ^{13}C-edited NOESY; 4D ^{13}C, ^{15}N-edited NOESY; and 4D ^{15}N, ^{15}N-edited NOESY spectra for an ILV methyl-protonated, otherwise perdeuterated, sample of calbindin D_{28k}. In the 3D ^{13}C, ^{13}C-edited NOESY spectrum (Fig. 9.10a), the autocorrelation peak for the γ-CH_3 group of Val62 can be seen at $F_1 = F_2 = 22.9$ ppm (^{13}C) and $F_3 = 1.38$ ppm (^{1}H). All other cross-peaks arise from NOE interactions with the Val62 $^{1}H^{\gamma}$ spins. The 4D ^{13}C, ^{15}N-edited NOESY in Fig. 9.10b shows NOEs from the Val62 $^{1}H^N$ spin to a variety of γ- and δ-methyl groups in the specifically protonated ILV sample. The slice is taken at the ^{15}N and $^{1}H^N$ shifts of Val62. The 4D ^{15}N, ^{15}N-edited NOESY in Fig. 9.10c shows the autocorrelation peak for the $^{1}H^N$–^{15}N group of Val62 at $F_1 = F_3 = 118.2$ ppm (^{15}N) and $F_2 = F_4 = 9.12$ ppm (^{1}H). All other peaks are NOE peaks from the Val62 $^{1}H^N$ spin.

The value of methyl-selective protonation in an otherwise perdeuterated environment has been demonstrated in the determination of global folds from a limited set of H^N–H^N, H^N–CH_3, and CH_3–CH_3 NOE restraints (*41, 66*). To some degree, however, both secondary structure and topology play roles in determining the quality of the structures that can be obtained from these limited NOE sets. This limitation is more evident for highly helical proteins, because long distances sometimes separate $^{1}H^N$ spins on adjacent helices (*41*). The relatively sparse NOEs available from perdeuterated and selectively protonated samples can be augmented by RDCs and anisotropic chemical shift changes measured in weakly aligned samples. Techniques for measurements of RDCs are described in Section 7.6. Kay and co-workers have determined the global fold of the 723-residue, 82-kDa enzyme malate synthase G using 746 H^N–H^N (99 long-range), 428 CH_3–CH_3 (386 long-range), and 357 H^N–CH_3 (142 long-range)

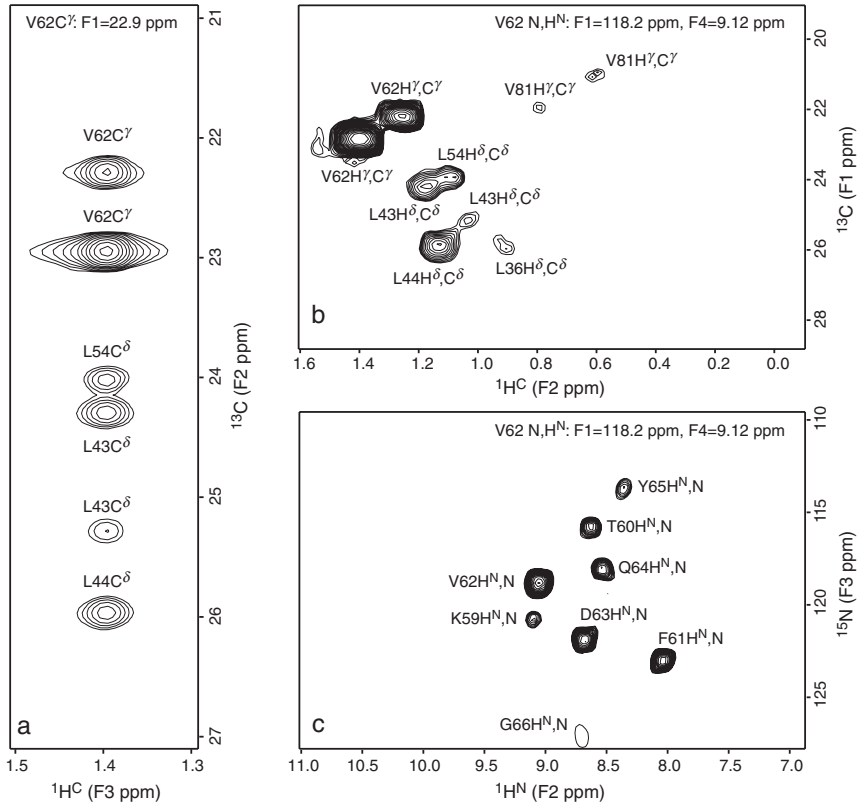

FIGURE 9.10 The 2D slices taken from (a) 3D $^{13}C/^{13}C$-separated NOESY, (b) 4D $^{13}C/^{15}N$-separated NOESY, and (c) 4D $^{15}N/^{15}N$-separated NOESY for a calbindin D_{28k} sample that is specifically protonated at the methyl groups of isoleucine, leucine, and valine and otherwise perdeuterated. The spectra were recorded on an 800-MHz NMR spectrometer. See text for details.

NOEs measured in isotropic solution together with 415 $^{1}H^{N}$–^{15}N RDCs and 300 ^{13}CO anisotropic chemical shift changes measured upon alignment of the protein using Pf1 phage (*67*).

Aromatic residues also are prevalent in the hydrophobic cores of proteins, and including distance restraints derived from aromatic ^{1}H NOEs can increase the accuracy of structures calculated from low-density NOE data sets (*68–70*). A biosynthetic method has been described for the selective proton labeling of Phe, Tyr, and Trp residues in perdeuterated proteins, using natural-abundance shikimic

acid (*32*). This approach selectively protonates aromatic rings, while the labeling of the backbone α- and side chain β-positions can be controlled independently via the D_2O and glucose added to the growth medium.

9.2 Intermolecular Interactions

Proteins interact with a variety of different types of ligands, including other proteins, peptides, DNA, RNA, small molecules, and metal ions. NMR methods together with differential isotope labeling strategies allow spectral information to be selectively acquired for individual, noncovalently linked constituents of multicomponent complexes (*5–7, 71–80*). Using these approaches, NMR spectroscopy can be used to detect binding of ligands to proteins, to identify the sites of ligand interactions on the surfaces of proteins, and to determine atomic-resolution molecular structures of protein–ligand complexes. The present discussion assumes that isotopically enriched molecules are available and that detailed structural information about the complex is to be obtained. Numerous techniques for detecting whether a given ligand interacts (weakly) with a target protein have been described, many of which do not require isotopic enrichment. These methods often are used in screening for potential lead compounds for pharmaceutical applications, rather than in structural studies [for reviews, see Carlomagno (*81*), Homans (*82*), and Pellechia et al. (*83*)].

9.2.1 Exchange Regimes

Whether a protein binds to its target ligand in a weak, intermediate, or strong fashion dictates not only the quality of the resulting NMR spectra, but also the information that those spectra can unambiguously provide. With this in mind, the *chemical exchange regime* for the system must be established before more detailed investigations can be undertaken (*84*). The following discussion follows the theoretical principles presented in Section 5.6.

The simplest kinetic scheme for binding of a ligand (L) to a protein (P) is described as a second-order exchange process,

$$\mathrm{P} + \mathrm{L} \underset{k_\mathrm{r}}{\overset{k_\mathrm{f}}{\rightleftharpoons}} \mathrm{PL}, \qquad [9.14]$$

in which k_f is the rate of the forward (association) reaction, k_r is the rate of the reverse (dissociation) reaction, and the chemical exchange lifetime, $\tau_{ex} = 1/k_{ex}$, is defined by

$$k_{ex} = k_f[L] + k_r. \qquad [9.15]$$

The three exchange regimes of interest are defined by

$$\begin{aligned} &\text{Slow exchange :} && k_{ex} \ll |\Delta\omega|, \\ &\text{Intermediate exchange :} && k_{ex} \sim |\Delta\omega|, \\ &\text{Fast exchange :} && k_{ex} \gg |\Delta\omega|, \end{aligned}$$

in which $\Delta\omega = \omega_P - \omega_{PL}$, and ω_P and ω_{PL} are the resonance frequencies of a nuclear spin in the uncomplexed and complexed protein, respectively.

The exchange regime for the protein–ligand system under investigation is determined by monitoring the changes in the protein NMR spectrum during a titration with ligand. The simplest approach monitors a well-resolved resonance in, for example, a 1D ^{1}H spectrum or a 2D ^{1}H–^{15}N correlation spectrum, with the proviso that the chosen peak must be detectably affected by the protein–ligand interaction. As the concentration of ligand is increased, changes in the spectrum (and the specific resonance in particular) provide information on the chemical exchange regime. In general, the following changes in the spectra potentially are observed:

1. A new protein resonance appears that increases in intensity but does not alter chemical shift as the ligand concentration increases. At the same time, the intensity of the resonance for the unliganded species decreases in intensity. Changes in linewidth are small. These observations imply a *slow exchange* process.
2. The protein resonance broadens significantly as ligand concentration is increased until it disappears when the total ligand concentration is approximately one-half that of the total protein concentration. The protein signal reappears at much higher ligand concentrations (perhaps in a different location). These observations imply an *intermediate exchange* process.
3. The protein resonance broadens notably at lower ligand concentrations, but becomes narrower at higher ligand concentrations. These observations imply a *moderately fast exchange* process.
4. The protein resonance does not change significantly in intensity or linewidth, but the chemical shift changes continuously as the ligand concentration increases. These observations imply a *fast exchange* process.

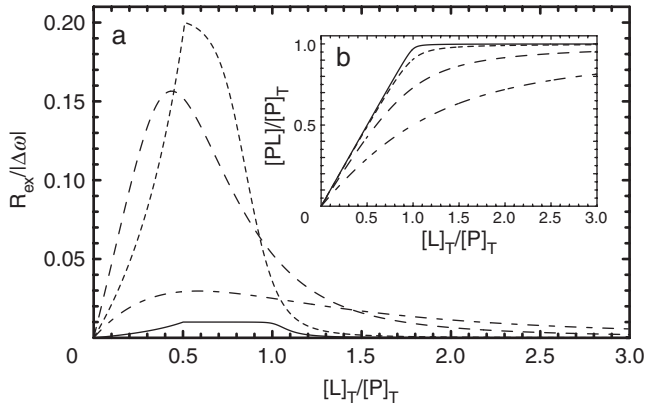

FIGURE 9.11 Ligand-induced contributions to chemical exchange linebroadening. (a) The chemical exchange contribution to transverse relaxation rate constant, R_{ex}, and (b) the degree of saturation of the protein binding site are shown as a function of total ligand concentration, $[L]_T$, for (—) $[P]_T = 1000K_d$ and $k_r = 0.01\Delta\omega$, (- - -) $[P]_T = 100K_d$ and $k_r = 0.2\Delta\omega$, (– – –) $[P]_T = 10K_d$ and $k_r = \Delta\omega$, and (– - – -) $[P]_T = 2K_d$ and $k_r = 5\Delta\omega$.

To provide a quantitative basis for these observations, calculated contributions to transverse relaxation resulting from chemical exchange are shown in Fig. 9.11. Rates of exchange are very dependent on solution conditions, including temperature, pH, and ligand concentration. These parameters must be known accurately and studies should be performed over a wide range of precisely monitored conditions.

Studies on proteins subject to intermediate exchange processes are particularly challenging, because line-broadening effects render resonances difficult, if not impossible, to detect. As a practical rule of thumb, the intermediate exchange regime frequently will be encountered when the dissociation constant (K_d) for the protein–ligand interaction is on the order of 10–100 μM.

9.2.2 PROTEIN–LIGAND BINDING INTERFACES

The exquisite sensitivity of NMR spectral parameters, including chemical shifts and relaxation rate constants, to molecular environments allows facile detection of intermolecular interactions of proteins with ligands. A large number of approaches have been developed

to efficiently identify the sites on a protein surface that interact with ligands. In some instances, the NMR observables can be used to guide modeling of the protein–ligand complex even in the absence of intermolecular structural restraints based on NOEs (*85, 86*). A selection of techniques in widespread use is discussed in the following sections.

9.2.2.1 Chemical Shift Mapping Perturbation of chemical shifts as a result of complex formation provides a highly sensitive tool for identification of protein binding sites. This procedure is referred to as *chemical shift mapping* and has been utilized in a variety of ways, including defining contacts between macromolecules and high-throughput screening of small ligands to determine structure–activity relationships (SARs) (*87*). Chemical shift mapping is especially valuable for studying weaker protein–ligand interactions in fast exchange ($K_d > 10^{-6}\,M$), because crystallization of such complexes is often difficult or impossible. Furthermore, large conformational changes of the protein, which could result in extensive changes to the NMR spectrum, usually do not occur in such weak binding interactions.

HSQC, TROSY, and other ^{1}H–^{15}N correlation spectra commonly are used for chemical shift mapping because these spectra are highly sensitive and often well-resolved. The binding surface on an ^{15}N-labeled protein is identified by titrating the unlabeled ligand into a solution of the protein and following the associated spectral changes in the ^{1}H–^{15}N correlation spectrum. Assignments for a complex in the fast-exchange regime are obtained by tracking the $^{1}H^{N}$ and ^{15}N resonances from their positions in the initial spectrum of the uncomplexed protein as the titration proceeds. When resonance positions no longer change with increasing ligand concentration, the protein is presumed to be saturated with ligand. The stoichiometry of protein–ligand binding is inferred from the titration endpoint. If the chemical exchange between the free and ligand-bound protein is slow, indicating a tightly bound complex, and/or if a large conformational change occurs upon binding, then chemical shift mapping is not as straightforward as in the fast-exchange limit, because reassignment of the protein resonances in the complex by standard approaches may be necessary.

Chemical shift changes often are quantified using the weighted chemical shift change per residue, Δ (*88*),

$$\Delta = [\Delta\delta_{H^N}^2 + (0.1\Delta\delta_N)^2]^{1/2}, \qquad [9.16]$$

in which $\Delta\delta_{H^N}$ and $\Delta\delta_N$ are the changes in chemical shifts of $^{1}H^{N}$ and ^{15}N, respectively, during complex formation, measured in units

of parts per million. The scaling factor of 0.1 is calculated from the ratio of the magnetogyric ratios ($\gamma_N/\gamma_H \sim 0.1$). The scaling factor empirically scales the ^{15}N chemical shift changes to be more equivalent to the ^{1}H chemical shift changes. If changes in ^{13}C chemical shifts are being monitored, a scaling factor of $\gamma_C/\gamma_H \sim 0.25$ is used. Scaling factors also can be estimated from the distribution of nucleus-specific chemical shift ranges in proteins (*88*). The dissociation constant for 1:1 binding equilibrium, K_d, can be estimated by fitting the observed chemical shift changes to the following equation:

$$\Delta = \Delta_{max}\left([L]_T + [P]_T + K_d - \left\{([L]_T + [P]_T + K_d)^2 - 4[L]_T[P]_T\right\}^{1/2}\right)/(2[P]_T), \quad [9.17]$$

in which Δ is the observed chemical shift change at a given total ligand concentration, $[L]_T$, (relative to the resonance frequency in the absence of ligand), Δ_{max} is the change in chemical shift at saturation and $[P]_T$ is the total protein concentration. However, because relatively high sample concentrations are required for NMR spectroscopy, dissociation constants are not easily measured for high-affinity complexes. Theoretical aspects of the determination of dissociation constants by NMR spectroscopy have been discussed (*89, 90*).

Resonances exhibiting large chemical shift changes upon ligand binding are assumed to reside at the binding interface. However, resonances in the spectrum may be shifted because the associated nuclei are proximal to the protein–ligand interface or because conformational changes upon binding have resulted in altered local magnetic environments, even for nuclear spins distant from the interaction site. These other local structural effects that would result in concomitant shift changes cannot be disregarded *a priori*, so caution is necessary to prevent overinterpretation of chemical shift perturbations. The key to discriminating between these two cases lies in establishing *intermolecular* NOE connectivities between the protein and the ligand (Section 9.2.4). Nevertheless, mapping of interfaces in this fashion is an excellent initial diagnostic.

9.2.2.2 Cross-Saturation Labeling strategies can be used together with cross-saturation methods to map interfaces in protein–ligand complexes (*91*). The method is generally applicable to large protein–protein complexes and, with minor modifications, to other protein–macromolecular ligand interactions — e.g., appropriately labeled DNA and RNA ligands (*92–94*).

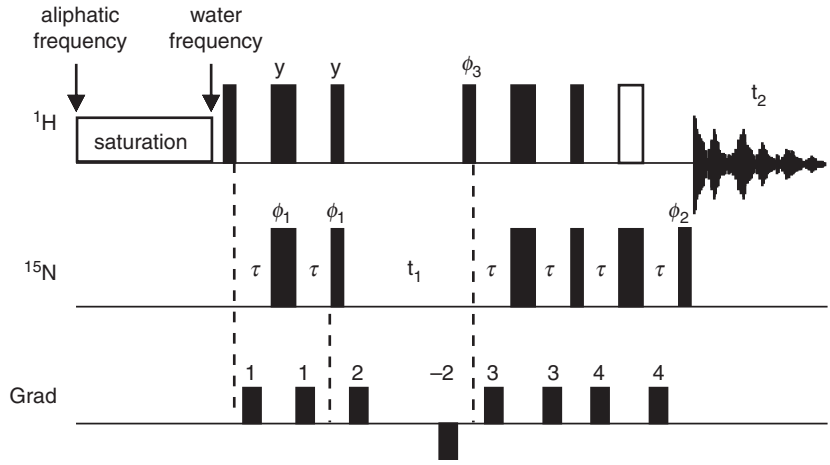

FIGURE 9.12 TROSY pulse sequence for using cross-saturation to determine protein–ligand interfaces. Thin and thick bars represent 90° and 180° pulses, respectively. The pulse depicted as an open bar is a 180° pulse crafted to leave the water magnetization unperturbed. Pulses are applied along the x-axis unless noted; $\tau = 1/(4J_{NH})$. Phase cycle is as follows: $\phi_1 = x, y, -x, -y$; $\phi_2 = y$; $\phi_3 = -y$; receiver $= x, y, -x, -y$ for the first FID. The second FID is acquired with $\phi_1 = x, y, -x, -y$; $\phi_2 = -y$; $\phi_3 = y$; receiver $= x, -y, -x, y$. Depending on the spectrometer, y and $-y$ phases may need to be interchanged. Band-selective saturation is applied in the middle of the aliphatic ^{1}H spectral region during the recycle delay. Frequency discrimination in the F_1 dimension is achieved as described in Section 7.1.3.3.

The simplest example is provided by a complex between two proteins. Protein A, regarded as the ligand, is produced unlabeled and fully protonated. Protein B, the protein whose binding interface is to be defined, is uniformly labeled with ^{2}H and ^{15}N. Protein A possesses a high density of ^{1}H spins, while protein B possesses a low density of ^{1}H spins. The physical basis of the technique is saturation transfer. The technique utilizes a variant of the water flip-back ^{1}H–^{15}N TROSY experiment (Section 7.1.4.2), as shown in Fig. 9.12. The experiment begins by irradiating the aliphatic region of the ^{1}H NMR spectrum (~0–3 ppm), while leaving the amide, aromatic, and water ^{1}H spins unperturbed. Such discrimination can be achieved by using a band-selective decoupling scheme such as WURST or CHIRP (*95–97*). Because protein B does not contain aliphatic ^{1}H spins, only protein A

initially is affected by the low-power rf field. Efficient spin diffusion through the high-density ^1H spin network causes rapid saturation of the aromatic and amide ^1H resonances of protein A. Thus, within a short period of time, the ^1H spectrum of protein A is fully saturated, while the amide $^1H^N$ spectrum of protein B is nearly unperturbed. However, because spin diffusion is effective for ^1H spins in close proximity, this condition does not persist. Although protein B is not directly affected by the irradiation, saturation of resonances in protein A is transferred across the intermolecular interface to proximal amide $^1H^N$ spins in protein B by the NOE. The low density of ^1H spins in protein B minimizes spin diffusion within the spin network of protein B and restricts saturation transfer effects to $^1H^N$ spins in the intermolecular interface. The reduction in intensities of $^1H^N$ resonances in protein B is measured by comparison to a reference spectrum acquired without irradiation of the aliphatic spectral region. Residues showing the largest difference in resonance intensity due to cross-saturation from protein A are identified as being located at the interface.

The method just described, although useful, has drawbacks, principally because cross-saturation is detected by the labile backbone amide $^1H^N$ spins. In order to make identification of the intermolecular interface as accurate as possible, the experiment should be performed in 90% D_2O to further isolate the amide $^1H^N$ spins and reduce spin diffusion in protein B. As a direct consequence, the overall sensitivity of the experiment is reduced approximately 10-fold. In addition, relatively few H^N atoms may be located in intermolecular interfaces, particularly for proteins with hydrophobic binding sites.

An improved version of this basic experiment takes advantage of the observation that methyl groups frequently are located at intermolecular interfaces (*98*). Cross-saturation between a fully protonated protein molecule and a methyl-protonated, otherwise perdeuterated, ligand offers significant sensitivity advantages. Perdeuteration ensures the required low ^1H spin density, methyl ^1H spins are nonexchangeable, and spin diffusion is intrinsically reduced by the favorable R_1 relaxation rate constants of the methyl ^1H spins.

9.2.2.3 Transverse Relaxation and Amide Proton Solvent Exchange Provided that the time scale for chemical exchange does not approach the very slow or very fast limits, then enhanced line broadening (or increase in R_2) frequently is observed for the resonances of nuclei at the binding interface of the protein–ligand complex. This effect is most easily observed for small to medium-sized proteins, because exchange results in only a small fractional increase in line

broadening (or R_2) for larger proteins with relatively broad lines in the absence of ligand. The advantage of this method, compared to mapping chemical shift perturbations, is that binding-induced structural rearrangements usually do not significantly increase linewidths or R_2 relaxation rate constants (provided that ligand binding is not associated with a change in oligomerization state of the protein).

Mapping of a protein–ligand interface also can be achieved by comparing the rates of amide–solvent hydrogen–deuterium exchange for the free and bound forms of the protein. $^{1}H^{N}$ and ^{15}N protein assignments must be known for the free and bound protein, and the largest effects usually are obtained for complexes in the slow exchange regime. Amide exchange rates are measured as described in Section 10.2.1.5. Amide $^{1}H^{N}$ spins in the complex that show *slower exchange* rates with solvent (enhanced protection) likely define regions of the protein involved in binding, because these spins are protected from solvent to an additional degree in the complex.

9.2.3 RESONANCE ASSIGNMENTS AND STRUCTURAL RESTRAINTS FOR PROTEIN COMPLEXES

The exchange regime for a protein–ligand complex governs the atomic resolution structural information that can be obtained for the protein, the ligand, and the protein–ligand interface. Again, the fast and slow chemical exchange regimes are the most amenable to detailed investigation.

If chemical exchange is slow (strong binding), then a stoichiometric complex between protein and ligand is suitable (in practice, the ligand may be titrated slightly past the stoichiometric ratio). The NMR resonances reflect the stoichiometric bound conformations of the protein and the ligand. In this regime, the complete structure of the protein–ligand complex can be determined based on intraprotein, intraligand, and interprotein–ligand NOE restraints (Section 9.2.4.2).

If exchange is fast, then the resulting NMR spectra characterize the average properties of the nuclear spins over an ensemble of possible states, depending on the protein:ligand ratio. The structure of the protein in the complex can be determined if the NMR observables are dominated by the properties of the protein in the complex, rather than by those of the free protein. To ensure this limit, sufficient excess ligand must be provided to saturate the protein binding site. In some cases, limited solubility of ligands may preclude reaching this limit. If exchange is fast, then protein–ligand NOEs usually will not be obtained.

In this regime, the transferred NOE can be used to determine structural characteristics of the ligand in its complexed form (*99–103*). The techniques described in Section 9.2.3 subsequently can be used to model the ligand–protein complex.

Resonance assignments and structural restraints for the protein component of a protein–ligand complex are obtained by recording the spectrum of the protein while suppressing resonances arising from the ligand, which otherwise would cause ambiguities and overlap. Selective observation of the NMR spectrum of one component of a complex is made possible by differential incorporation of isotopic labels into the protein and ligand. In the experimental design considered herein, the protein is labeled, typically with ^{15}N and ^{13}C, and the ligand is unlabeled. In some cases, different isotopes are incorporated into the protein and the ligand (i.e., one component of the complex might be labeled with ^{13}C and the other component might be labeled with ^{15}N). In either situation, the protein and ligand molecules can be regarded as independent from an NMR viewpoint.

9.2.3.1 Assignments and Structures of Proteins in Protein–Ligand Complexes If the protein component of a protein–ligand complex is doubly labeled with $^{15}N/^{13}C$ or triply labeled with $^{2}H/^{13}C/^{15}N$, then the standard multidimensional heteronuclear NMR experiments described in Chapters 7 and 9 (see Section 9.1) are employed to obtain backbone and side chain assignments, stereospecific assignments, and torsion angle restraints solely for the protein in its complexed form. Four types of NOE cross-peaks can be expected for a binary complex consisting of labeled ($^{15}N/^{13}C$) protein (P) and unlabeled ($^{12}C/^{14}N$) ligand (L):

$$\begin{aligned} &\text{Intramolecular:}\quad P(^{15}N/^{13}C) \rightarrow P(^{15}N/^{13}C), \quad L(^{12}N/^{14}C) \rightarrow L(^{12}N/^{14}C). \\ &\text{Intermolecular:}\quad P(^{15}N/^{13}C) \rightarrow L(^{12}N/^{14}C), \quad L(^{12}N/^{14}C) \rightarrow P(^{15}N/^{13}C). \end{aligned} \qquad [9.18]$$

For structure determination of the protein, those NOEs that provide structural information for the labeled protein alone are of interest.

NOEs between ^{1}H spins of the labeled protein are easily established because only those signals that originate or terminate on the unlabeled ligand must be suppressed. However, conventional 3D ^{15}N- or ^{13}C-edited NOESY experiments (Sections 7.2.1 and 7.2.3) ordinarily will not suffice, because these experiments generally only employ one heteronuclear filter. In the final NOESY spectrum, NOEs appear between ^{1}H spins attached to isotopically labeled nuclei and *all* other

proximal ^{1}H spins, whether they are attached to isotopically labeled nuclei or not. Consequently, both intra- and intermolecular NOEs are present in the spectrum.

To ensure suppression of cross-peaks generated by intermolecular NOEs, NOESY experiments must select for heteronuclear coherences both *before* and *after* the NOESY mixing time. The only NOEs observed occur between ^{1}H nuclei that are directly attached to isotopically labeled heteronuclei (those in the protein). For example, the 3D ^{1}H–^{15}N HMQC–NOESY–HMQC experiment (Section 7.2.4.1) can be used to provide NOEs between amide $^{1}H^{N}$ spins in the protein alone. The only modification to the sequence required is to introduce ^{13}C 180° decoupling pulses at $t_1/2$ and $t_2/2$, assuming a doubly labeled protein. Similarly, the 4D $^{13}C/^{15}N$ HMQC–NOESY–HMQC experiment (Section 7.2.4.2) provides NOEs between ^{13}C-bound ^{1}H spins and ^{15}N-bound ^{1}H spins exclusively, rejecting any interference from unlabeled ligand ^{1}H spins. The 4D $^{13}C/^{13}C$ HMQC–NOESY–HMQC (Section 7.2.4.3), with ^{15}N decoupling applied throughout the sequence, can be used to generate NOEs between ^{13}C-bound protons within the protein exclusively.

The ^{13}C 3D HSQC–NOESY experiment can be used to generate intraprotein NOE correlations for a protein–ligand complex if the protein is labeled with ^{13}C, while the ligand is perdeuterated, but not labeled with $^{15}N/^{13}C$. This is straightforward if the ligand is another protein that can be easily obtained biosynthetically by overexpression. In 100% D_2O buffer, intermolecular ^{1}H–^{1}H NOEs cannot be generated and only intramolecular $^{1}H(^{13}C)$–$^{1}H(^{13}C)$ NOEs are observed.

9.2.3.2 Isotope-Edited/Filtered NOESY to Define Intermolecular Interfaces Accurately identifying and determining the atomic resolution structure of the interface in a protein–ligand complex requires establishing unambiguous intermolecular restraints between the protein and ligand. The following discussion focuses on isotope-filtered techniques for establishing NOE connectivities between the protein and the ligand; however, RDCs (*104–106*) and trans-hydrogen scalar coupling interactions (*107*) also potentially provide intermolecular restraints. Isotope-filtered methods have been reviewed (*108, 109*).

Identifying intermolecular NOEs depends on techniques to selectively observe the NMR spectra of individual components of the protein–ligand complex based upon the differential incorporation of isotopic labels into the components of a molecular complex. In the present discussion, the protein is assumed to be labeled and the ligand is assumed to be unlabeled; in practice, the opposite labeling strategy

might be used as well (particularly for investigations of protein–nucleic acid complexes). The pulse sequence for separating the NMR spectrum into individual subspectra of isotopically enriched or natural-abundance components is referred to as an *isotope filter* and is constructed from a heteronuclear spin echo difference experiment. The pulse sequence can be used to either *select* signals from the isotopically labeled species while *suppressing* signals from nonlabeled entities, normally referred to as isotope editing, or can be used to *reject* signals from the isotopically labeled species while *retaining* signals from nonlabeled entities, normally referred to as isotope filtering (*109–121*).

The most straightforward experiment for these applications is referred to as a *half-filter*. Half-filters often are combined with full NOESY experiments to generate subspectra that contain different types of NOE cross-peaks. The basic half-filter is (*122*)

$$\begin{aligned} {}^1\mathrm{H}: &\quad 90_x - \tau - 180_x - \tau -, \\ \mathrm{X}: &\quad\quad\quad 90_x 90_\phi, \end{aligned} \qquad [9.19]$$

in which $\tau = 1/(2^1J_{IS})$ Because $^1J_{CH}$ and $^1J_{NH}$ are significantly larger than $^3J_{HH}$, evolution of the ^{1}H–^{1}H scalar coupling interaction during τ is considered negligible. The pulse sequence is executed twice, once with $\phi = x$ and once with $\phi = -x$. The ^{1}H spins that are not coupled to a heteronucleus (designated by the operator K) do not experience the effects of the pulses on the X nucleus (designated by the operator S). Evolution through the half-filter yields

$$K_z \rightarrow K_y \qquad [9.20]$$

for both transients. The ^{1}H spins that are coupled to a heteronucleus (designated by the operator I) evolve under the heteronuclear coupling Hamiltonian and experience the effects of the pulses on the X nucleus. Evolution through the half-filter yields

$$\begin{aligned} I_z &\xrightarrow{\frac{\pi}{2}I_x} -I_y \xrightarrow{{}^1J_{IS}} -I_y\cos(\pi {}^1J_{IS}\tau) + 2I_xS_z\sin(\pi {}^1J_{IS}\tau) \\ &\xrightarrow{\pi I_x, \frac{\pi}{2}S_x, \frac{\pi}{2}S_\phi} I_y\cos(\pi {}^1J_{IS}\tau) - \mathrm{sgn}(\phi)2I_xS_z\sin(\pi {}^1J_{IS}\tau) \\ &\xrightarrow{{}^1J_{IS}} I_y[\cos^2(\pi {}^1J_{IS}\tau) - \mathrm{sgn}(\phi)\sin^2(\pi {}^1J_{IS}\tau)] \\ &\quad - 2I_xS_z[1 + \mathrm{sgn}(\phi)]\sin(\pi {}^1J_{IS}\tau)\cos(\pi {}^1J_{IS}\tau), \end{aligned} \qquad [9.21]$$

in which sgn(ϕ) is +1 when $\phi = x$ and −1 when $\phi = -x$. Adding the two transients together selects for resonances of ^{1}H nuclei *not* coupled to X nuclei, yielding an isotope-filtered spectrum:

$$K_z + I_z \rightarrow K_y + I_y \cos^2(\pi\, {}^1J_{IS}\tau). \qquad [9.22]$$

Subtracting the two scans selects for resonances of ^{1}H nuclei that *are* coupled to a heteronucleus, yielding an isotope-edited spectrum:

$$K_z + I_z \rightarrow -I_y \sin^2(\pi\, {}^1J_{IS}\tau). \qquad [9.23]$$

The antiphase operators have been ignored in writing [9.22] and [9.23] because these terms normally are suppressed or rendered unobservable by other pulse sequence elements in the complete experiment.

The level of suppression of the *S*-bound *I*-spin magnetization achieved in the isotope-filtered subspectrum is proportional to $\cos^2(\pi {}^1J_{IS}\tau)$. Filtering is perfect for a nominal coupling constant ${}^1J^0_{IS} = 1/(2\tau)$. For other scalar coupling constants, the intensity of the residual I_y magnetization that survives the filter is given by

$$\begin{aligned}\varepsilon &= \cos^2(\pi {}^1J_{IS}\tau) = \cos^2(\pi {}^1J_{IS}/[2\,{}^1J^0_{IS}]) = \sin^2(\pi \Delta J/[2\,{}^1J^0_{IS}]) \\ &\approx (\pi^2/4)(\Delta J/{}^1J^0_{IS})^2, \end{aligned} \qquad [9.24]$$

in which $\Delta J = {}^1J_{IS} - {}^1J^0_{IS}$. The filter depends on two delays of nominal length $1/(2\,{}^1J^0_{IS})$ and results in filter breakthrough errors proportional to ΔJ^2, for small variations in the scalar coupling constant. A filter with this property is referred to as a "second-order *J*-filter." As shown by [9.23], variation in the scalar coupling constants reduces the sensitivity of isotope-edited experiments, but does not result in breakthrough peaks.

In actual practice, the two transients for the isotope filter in [9.19] might be acquired in a different fashion. For the first transient, the $90^\circ_x 90^\circ_x$ ^{13}C pulse combination is replaced by a composite 180° pulse to minimize pulse imperfections and effects of resonance offset. For the second transient, the $90^\circ_x 90^\circ_{-x}$ ^{13}C pulse combination is omitted.

Breakthrough peaks in the isotope-filtered subspectrum are particularly troublesome for ^{1}H–^{13}C isotope-filtered experiments. Perfect discrimination between ^{1}H atoms bound to ^{13}C or ^{12}C atoms relies on the delay τ being perfectly matched to the $^1J_{CH}$ coupling. This coupling constant is far from uniform. For example, aromatic ^{13}C nuclei have $^1J_{CH}$ in the range 160–180 Hz, ^{13}C nuclei attached to nitrogen or oxygen atoms have $^1J_{CH} \sim 140$ Hz, and ^{13}C nuclei in a methyl group have $^1J_{CH} \sim 125$ Hz. Therefore, the isotope-filter delay cannot be tuned

simultaneously for all $^1J_{CH}$ values. The resulting unwanted signals in the subspectra increase overlap and cause ambiguities in spectral interpretation.

In principle, any ^{1}H NMR experiment can be modified to incorporate the half-filter element. For example, an ω_1 half-filtered NOESY experiment is obtained by replacing the first 90° pulse in an ^{1}H 2D NOESY pulse sequence with the half-filter element (*112*). The basic experiment is written as follows:

$$\begin{array}{lcccccc} ^1\text{H:} & 90_x\text{–}\tau\text{–}180_x\text{–}\tau\text{–}t_1/2\text{–}t_1/2\text{–}90_x\text{–}\tau_m\text{–}90_x\text{–receiver} \\ \text{X:} & & 90_x 90_\phi & & 180_x & & \text{decouple} \end{array} \qquad [9.25]$$

Appropriate construction of the phase cycle to subtract alternate scans ensures that only ^{1}H spins attached to, for instance, ^{15}N enter into the t_1 period. In this case, the resulting spectrum would include only NOE cross-peaks having resonance frequencies of $^1H^N$ in the indirect dimension, but *all* proximal ^{1}H spins in the direct dimension. The complementary ω_2 half-filtered NOESY (*123*) replaces the final 90° pulse in an ^{1}H NOESY experiment with the half-filter element and provides a full complement of NOEs in the indirect dimension and, with suitable phase cycling, only $^1H^N$ spins in the direct dimension.

The ω_1 and ω_2 half-filter experiments are combined in the *double-half-filter* experiment (*117*). A pulse sequence for a 2D ^{1}H–^{1}H NOESY experiment with a $^{13}C(F_1, F_2)$-double-half-filter is shown in Fig. 9.13. The sequence consists of two half-filter elements surrounding a NOESY experiment. The two pairs of $90^\circ_x 90^\circ_{\psi 1}$ and $90^\circ_x 90^\circ_{\psi 3}$ pulses on the ^{13}C spin are phase cycled independently in combination with the receiver to generate four data sets that are recorded separately. Linear combinations of the four sets of data provide for an elegant editing scheme that allows each of the four types of NOEs listed in [9.18] to be independently observed. Table 9.2 summarizes the processing scheme and the information content of the four sets of subspectra. Intermolecular NOEs between the protein and the ligand are present in two of the subspectra, reflecting magnetization transfer originating on a protein ^{1}H spin or originating on a ligand ^{1}H spin. If the protein assignments are known, then the precise location of the protein interface can be determined.

A practical issue concerns 1D versus *n*D isotope-edited NMR experiments. Sometimes, a 1D isotope-edited experiment would, in principle, suffice for a given application (for example, monitoring the resonances of a small labeled ligand bound to a large unlabeled protein). In practice, the large natural-abundance ^{13}C signal from the protein can

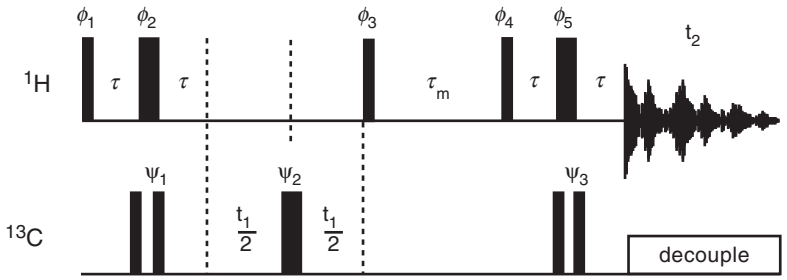

FIGURE 9.13 Basic pulse sequence for a ^{13}C-double-half-filter NOESY experiment. Thin and thick bars represent 90° and 180° pulses, respectively. Pulses are applied along the x-axis unless noted. Phases ϕ_1–ϕ_5 and ψ_2 are all alternated independently from x to $-x$; concomitantly, the receiver phase is alternated with each phase shift of a 90° pulse. Four combinations of this sequence are acquired: (1) $\psi_1 = \psi_3 = x$; (2) $\psi_1 = -x$, $\psi_3 = x$; (3) $\psi_1 = x$, $\psi_3 = -x$; and (4) $\psi_1 = \psi_3 = -x$. Subspectra are generated as noted in Table 9.2.

TABLE 9.2
Processing Schemes and Information Content for Double-Half-Filtered NOESY

Linear combination[a]	Subspectrum type	Information content
$1+2+3+4$	$^{13}C(F_1)$–$^{13}C(F_2)$, doubly filtered	**Intramolecular** NOEs between ^{1}H spins in unlabeled ligand
$1-2-3+4$	$^{13}C(F_1)$–$^{13}C(F_2)$, doubly selected	**Intramolecular** NOEs between ^{1}H spins in ^{13}C-labeled protein
$1-2+3-4$	$^{13}C(F_1)$–$^{13}C(F_2)$, F_1 selected–F_2 filtered	**Intermolecular** NOEs between ^{1}H spins in unlabeled ligand (F_2) and ^{1}H spins in ^{13}C-labeled protein (F_1)
$1+2-3-4$	$^{13}C(F_1)$–$^{13}C(F_2)$, F_1 filtered–F_2 selected	**Intermolecular** NOEs between ^{1}H spins in ^{13}C-labeled protein (F_2) and ^{1}H spins in unlabeled ligand (F_1)

[a]Phase cycles used for data sets 1–4 are given in the caption to Fig. 9.13.

be a major impediment. In such cases, a 2D (or higher dimensionality) experiment is needed to disperse the natural-abundance signals so that the ligand resonances can be observed (*124*).

The half-filter sequence given in [9.19] is a difference experiment and, as such, relies on extremely high spectrometer stability (just like phase cycling). Isotope filtration that does not rely on a phase-cycled difference experiment is obtained by incorporating spin lock purge pulses or gradient pulses into the pulse sequence elements. A variation of the basic half-filter that uses purge pulses to obtain isotope filtering is represented as follows (*125*):

$$\begin{array}{ll} {}^1\mathrm{H}: & 90_x\text{–}\tau/2\text{–}180_x\text{–}\tau/2\text{–}[\text{spin lock}]_y \\ \mathrm{X}: & \qquad\qquad 180_x \qquad 90_x \end{array} \qquad [9.26]$$

After a total delay of $\tau = 1/(2^1J_{\mathrm{XH}})$, prior to the spin lock pulse and the 90°(S) pulse, evolution of magnetization is described by

$$K_z + I_z \rightarrow K_y + I_y \cos(\pi {}^1J_{IS}\tau) - 2I_xS_z \sin(\pi {}^1J_{IS}\tau). \qquad [9.27]$$

The 90°(*S*) pulse converts the antiphase coherence to multiple-quantum coherence and the spin lock applied to the ^{1}H spins both dephases the multiple-quantum coherence and retains in-phase ^{1}H magnetization. The total time for this filter (neglecting the duration of the spin lock) is one-half that of the basic half-filter; thus, losses due to relaxation also are reduced. In contrast to [9.19], no phase cycling is required for this filter sequence.

For the simple half-filter element described in [9.26], the level of suppression of the *S*-bound *I*-spin magnetization is dependent on $\cos(\pi {}^1J_{IS}\tau)$. The intensity of the residual I_y magnetization that survives the filter is given by

$$\begin{aligned} \varepsilon &= \cos(\pi {}^1J_{IS}\tau) = \cos(\pi {}^1J_{IS}/[2{}^1J^0_{IS}]) = -\sin(\pi \Delta J/[2{}^1J^0_{IS}]) \\ &\approx -(\pi/2)(\Delta J/{}^1J^0_{IS}). \end{aligned} \qquad [9.28]$$

The filter depends on only the one delay, and results in filter breakthrough errors proportional to ΔJ, for small variations in the scalar coupling constant. Thus, this filter is referred to as a "first-order *J*-filter."

Various schemes are available to increase the degree of suppression achieved by isotope filters, particularly for ^{1}H–^{13}C spin pairs; first-order filters normally are sufficient for application to amide ^{1}H–^{15}N spin pairs.

A simple example of a second-order filter using spin lock purge pulses is obtained from the addition of two first-order filters (*48, 118, 125*):

$$\begin{array}{lllllll} {}^{1}\mathrm{H}: & 90_x\text{–}\tau_1/2\text{–}180_x\text{–}\tau_1/2\text{–}[\text{spin-lock}]_y\text{–}\tau_2/2\text{–}180_x\text{–}\tau_2/2\text{–}[\text{spin-lock}]_y & & & & & \\ {}^{13}\mathrm{C}: & & 180_x & 90_\phi & & 180_x & 90_{\phi-90^\circ} \end{array} \qquad [9.29]$$

The values of τ_1 and τ_2 are set to accommodate different ${}^{1}J_{\mathrm{CH}}$ couplings, e.g., $\tau_1 = 3.57$ ms (${}^{1}J_{\mathrm{CH}} = 140$ Hz) and $\tau_2 = 4.0$ ms (${}^{1}J_{\mathrm{CH}} = 125$ Hz). The overall level of suppression during this sequence is given by $\cos(\pi {}^{1}J_{\mathrm{CH}}\tau_1)\cos(\pi {}^{1}J_{\mathrm{CH}}\tau_2)$. Higher order filters provide efficient suppression of undesired magnetization over a wider range of ${}^{1}J_{\mathrm{CH}}$ scalar coupling constants; however, the sequences are longer and relaxation losses are greater.

A simple second-order filter that utilizes pulsed field gradients is

$$\begin{array}{lllll} {}^{1}\mathrm{H}: & 90_x - \tau - 180_x - \tau - & & & \\ {}^{13}\mathrm{C}: & & 90_x & 90_x & \\ \text{Grad}: & & \text{g1} & g1 & \end{array} \qquad [9.30]$$

Magnetization for ^{1}H spins not coupled to a ^{13}C spin is unaffected by the ^{13}C pulses and forms a gradient echo. Magnetization for ^{1}H spins coupled to a ^{13}C spin evolves into antiphase coherence during the first delay τ, is converted to multiple-quantum coherence by the first ^{13}C 90° pulse, and is dephased by the second gradient g1. Residual I_y magnetization evolves into antiphase coherence during the second delay τ and is converted to multiple-quantum coherence by the second ^{13}C 90° pulse. The overall level of suppression during this sequence is given by $\cos^2(\pi {}^{1}J_{\mathrm{CH}}\tau)$.

Replacing the hard 180°(^{13}C) pulses in half-filter elements by designed adiabatic inversion pulses is an elegant approach to increase the level of suppression (*126, 127*). The scalar coupling constants ${}^{1}J_{\mathrm{CH}}$ are roughly linearly correlated with ^{13}C chemical shifts. Thus, by judicious choice of the sweep rate and field strength of the adiabatic inversion pulse (Section 3.4.6), suppression errors caused by the mismatch of the filter timing with respect to ${}^{1}J_{\mathrm{CH}}$ are minimized. Another method providing improved suppression takes advantage of the similarity between composite pulse rotations and broadband polarization transfer and does not rely on relationships between ^{13}C shifts and ${}^{1}J_{\mathrm{CH}}$ values (*128*). The scaling for this third-order filter is proportional to

$\cos^3(\pi {}^1J_{CH}\tau)$, in which $\tau = 1/(2{}^1J_{CH})$. This filter has been shown to provide good suppression over a range 115 to 165 Hz (when τ is set for ${}^1J^0_{CH} = 140$ Hz) and, as such, provides excellent purging for all ^{1}H atoms attached to ^{13}C atoms in a protein, apart from those in histidine imidazole groups.

Isotope-filter elements can be implemented in any dimension of a multidimensional experiment as deemed appropriate. For example, an F_1-edited, F_3-filtered ^{13}C 3D HMQC–NOESY experiment has been used to assign intermolecular NOEs between isotopically labeled and unlabeled components of a complex (*129*).

9.3 Methods for Rapid Data Acquisition

As the discussions in Chapters 6–8 make clear, a large number of NMR spectra might be recorded in the course of a single investigation of the structure, dynamics, and interactions of a protein. Recording the necessary multidimensional NMR data sets represents a significant investment of spectrometer time; therefore, efficiency in collecting data is an important issue in biomolecular NMR spectroscopy. In particular, the inherent sensitivity of NMR spectrometers has steadily increased as a result of developments in magnet, probe, and amplifier technology and the total number of transients that must be recorded to achieve a given signal-to-noise ratio decreases with each improvement in spectrometer sensitivity. Many modern gradient-enhanced heteronuclear multidimensional NMR experiments already use minimal phase cycling, typically consisting only of isotope editing and quadrature detection. In this limit, the total length of the NMR experiment is determined by the requirements of the Nyquist sampling theorem and the maximum evolution times in indirect dimensions needed for resolution. Further reduction in total experimental data acquisition times requires new methods for recording NMR spectra.

Certain techniques that potentially provide two- to fourfold reductions in experimental data acquisition time already are in common use. Techniques for optimizing recovery of magnetization between transients allow individual transients to be recorded more rapidly (*45–47*). Aliasing in ^{13}C frequency dimensions enables long evolution times to be achieved in a smaller number of increments, which enables highly resolved spectra to be acquired more rapidly (Sections 7.1.2.3 and 7.1.5). Linear prediction and maximum entropy reconstruction methods can improve resolution for spectra recorded with limited digital resolution (Section 3.3.4). In some cases, more than one type of correlation can be

recorded in a single NMR experiment. The simultaneous $^{13}C/^{15}N$-edited NOESY experiment is an important example in biomolecular NMR (*130*). Atreya and Szyperski review many of these approaches (*131*).

Emerging methods seek to minimize experimental data acquisition times by dramatically reducing the number of transients that must be recorded to obtain the necessary spectral resolution. These methods avoid the strictures imposed by the conventional sampling strategy in which multidimensional NMR experiments are recorded by systematically and independently incrementing each of the indirect evolution delays. Three of these methods, nonuniform sampling, GFT, and projection–reconstruction, are briefly discussed here in order to provide an introduction to the field. These and other approaches, including filter diagonalization (*132–134*), single-scan NMR (*135, 136*), and Hadamard spectroscopy (*137–139*), have been discussed in reviews by Freeman and Kupče (*140, 141*).

9.3.1 NONUNIFORM SAMPLING

The most intuitive approach relaxes the requirement that indirect frequency dimensions are sampled at regular increments. This requirement is imposed by the conventional fast Fourier transformation algorithm (Section 3.3.1); however, this sampling strategy means that transients with low signal-to-noise ratios are recorded whenever one or more of the indirect evolution periods are long. Nonuniform sampling uses more extensive recording of data for smaller values of the indirect evolution delays (when sensitivity is high) and less extensive recording for larger values of the evolution delays (when sensitivity is low). The sampling scheme is designed to maximize resolution and signal-to-noise ratio within a given total experimental data acquisition time (*142*). Nonuniform sampled data cannot be processed by conventional Fourier transformation algorithms. Maximum entropy reconstruction (*142*), Fourier transform algorithms for nonequispaced data (*143*), and multidimensional decomposition (*144*) have been used to process spectra recorded with nonuniform sampling in indirect evolution periods. Two- to sixfold reductions in experimental data acquisition times have been demonstrated (*142, 144*). A particularly powerful illustration of this approach, combined with other techniques discussed in Section 9.1, is provided by a 4D ^{13}C, ^{13}C-edited NOESY spectrum recorded using a methyl-protonated, otherwise perdeuterated, sample of malate synthase G (723 residues, 82 kDa) (*145*). Data acquisition used methyl-TROSY techniques and nonuniform sampling to optimize

sensitivity and resolution. The spectrum was processed using multidimensional decomposition.

9.3.2 GFT-NMR SPECTROSCOPY

The G-matrix Fourier transform NMR (GFT-NMR) was introduced by Kim and Szyperski in 2003 (*146*) and is comprehensively reviewed by Atreya and Szyperski (*131*) and by Freeman and Kupče (*140*). GFT employs the so-called reduced dimensionality (RD) principle in which multiple indirect evolution periods are incremented simultaneously, rather than independently (*147–155*). The initial report of GFT-NMR has been followed by additional developments and demonstrations (*156–159*) as well as applications to protein assignments and structure determination (*160, 161*).

A GFT-NMR experiment co-evolves m indirect evolution periods of an nD experimental pulse sequence using the RD technique. The resulting data set is referred to as an $(n, n - m + 1)$D GFT-NMR spectrum. For example, t_1 and t_2 indirect evolution times are defined by $t_1 = t$, $t_2 = \kappa t$, in which κ is a constant that allows for different spectral widths in the different frequency dimensions ($\kappa = 1$ in the simplest implementation), in a (3, 2)D GFT-NMR experiment. A GFT-NMR data set consists of 2^m RD NMR experiments in which sine- and cosine-modulated data for each of the co-evolved indirect dimensions are collected by modulating the phases of the appropriate pulses in the sequence. For example, in a (3, 2)D GFT-HNCA experiment, four data sets are acquired in which the 90° pulse before t_1 and the 90° pulse before t_2 have phases $\{x, x\}$, $\{x, y\}$, $\{y, x\}$, and $\{y, y\}$; these are the same sets of phase shifts that would be required for quadrature detection in the two indirect evolution periods of a conventional data acquisition. The resulting time-domain signals in the indirect dimensions are given by

$$\begin{aligned} s_A(t) &= \cos(\Omega_1 t)\ \cos(\Omega_2 \kappa t), \quad s_C(t) = \sin(\Omega_1 t)\ \cos(\Omega_2 \kappa t); \\ s_B(t) &= \cos(\Omega_1 t)\ \sin(\Omega_2 \kappa t), \quad s_D(t) = \sin(\Omega_1 t)\ \sin(\Omega_2 \kappa t). \end{aligned} \qquad [9.31]$$

The GFT method unravels the chemical shift information from the intertwined indirect evolution times by addition or subtraction of the individual sets of frequency-domain data. In the present example, the two spectra, represented by

$$s_A(t) + s_D(t) = \cos([\Omega_1 - \kappa\Omega_2]t), \quad s_B(t) - s_C(t) = \sin([\Omega_1 - \kappa\Omega_2]t), \qquad [9.32]$$

represent a phase-sensitive 2D data set in which resonance signals appear at frequency positions $\Omega_1 - \kappa\Omega_2$ in the indirect dimension. The two spectra, represented by

$$s_A(t) - s_D(t) = \cos([\Omega_1 + \kappa\Omega_2]t), \quad s_B(t) + s_C(t) = \sin([\Omega_1 + \kappa\Omega_2]t), \tag{9.33}$$

represent a phase-sensitive 2D data set in which resonance signals appear at frequency positions $\Omega_1 + \kappa\Omega_2$ in the indirect dimension. In principle, the resonance frequencies for cross-peaks in a conventional 3D experiment are obtained equivalently in (3, 2)D GFT-NMR by adding and subtracting the frequencies of the resonance pairs in these two 2D spectra. In practice, identifying the corresponding resonances in congested spectra is facilitated by acquiring additional lower dimensionality spectra with fewer co-evolved evolution periods. In the example being discussed, a conventional 2D spectrum that records only the frequency Ω_1 in the indirect dimension enables the cross-peaks with frequencies $\Omega_1 - \kappa\Omega_2$ and $\Omega_1 + \kappa\Omega_2$ to be identified unambiguously by symmetry with respect to the cross-peak with frequency Ω_1. Thus, in this example, a total of six 2D data sets is acquired to generate the information that would be obtained from a conventional 3D experiment with k sampled points in the third dimension (requiring acquisition of a total of $2k$ 2D spectra for quadrature detection). For $k = 32$, the GFT-NMR data set requires only one-tenth the number of 2D acquisitions. The 2D RD data sets for GFT-NMR may need to be acquired with increased numbers of points in the indirect dimensions to achieve sufficient resolution and/or increased numbers of transients to achieve acceptable signal-to-noise ratios compared to the individual 2D planes from the conventional 3D spectrum. Nonetheless, even accounting for these issues, considerable savings in data acquisition time are achievable by GFT-NMR.

As indicated by the preceding example, the GFT method provides large reductions in data acquisition times for higher dimensionality experiments. Resonance signal overlap, as is often the case in the spectra of larger proteins, can result in difficulties in obtaining clean frequency separation in GFT data sets. Enhanced resolution can be obtained by increasing the number of frequency dimensions; however, each additional dimension in GFT-NMR splits the resonance signals into a doublet and sensitivity drops accordingly. GFT has been incorporated into a highly efficient streamlined protocol for structure determination of proteins < 20 kDa (*161*).

9.3.3 PROJECTION–RECONSTRUCTION

Kupče and Freeman have introduced projection–reconstruction (PR), a method widely used in disparate fields, including X-ray tomography, medical imaging, and astronomy to the field of protein NMR spectroscopy (*162–168*). Kupče and Freeman demonstrated that full 3D and 4D spectra can be reconstructed from a small set of 2D spectra recorded at various "tilt angles." Using the terminology of reduced dimensionality (GFT), these experiments are generally referred to as (3, 2)D PR-NMR and (4, 2)D PR-NMR data sets.

The PR method, like GFT, co-evolves each of the indirect evolution times. The relative sizes of the incrementable evolution delays are chosen to generate a projection of the spectrum onto a plane inclined at a predefined angle (the "tilt angle"). PR is based on a Fourier transform theorem that states that a section through the origin of a two-dimensional time-domain signal, $s(t_1, t_2)$, inclined at an angle, α, with respect to the t_1 axis, transforms as the projection of the corresponding frequency-domain spectrum $S(F_1, F_2)$ onto an axis through the origin inclined at the same angle. For (3, 2)D PR-NMR experiments, t_1 and t_2 indirect evolution times are defined by $t_1 = t \cos\alpha$, $t_2 = t \sin\alpha$ to generate a projection onto a plane rotated around the F_3 axis, subtending an angle α with respect to the F_1–F_3 plane [the extension to (4, 2)D PR-NMR experiments is straightforward]. For each tilt angle in a (3, 2)D PR-NMR experiment, two projections are collected (positive and negative angles), both of which provide independent information about cross-peaks in the spectrum. The key is to record enough tilted planes to define the position of cross-peaks accurately, but not so many that the time required experimentally becomes large. Criteria for this choice have been discussed (*169, 170*). In PR-NMR, unlike GFT-NMR, the data are reconstructed to form a conventional NMR spectrum; therefore, chemical shift information does not need to be unraveled by multiple additions and subtractions. In addition, cross-peaks are not split into pairs by each additional co-evolved dimension; therefore, sensitivity is not substantially degraded by adding additional dimensions.

A number of different algorithms have been proposed to reconstruct the NMR spectrum from a set of projections, and research in this area continues. The Lower-Value (LV) reconstruction algorithm, introduced by Kupče and Freeman, is well-suited for data sets containing relatively few highly dispersed signals (*165*). However, the intensities of the reconstructed peaks are determined by the signal-to-noise ratio of the weakest of the projections, and the signal-to-noise ratio of the

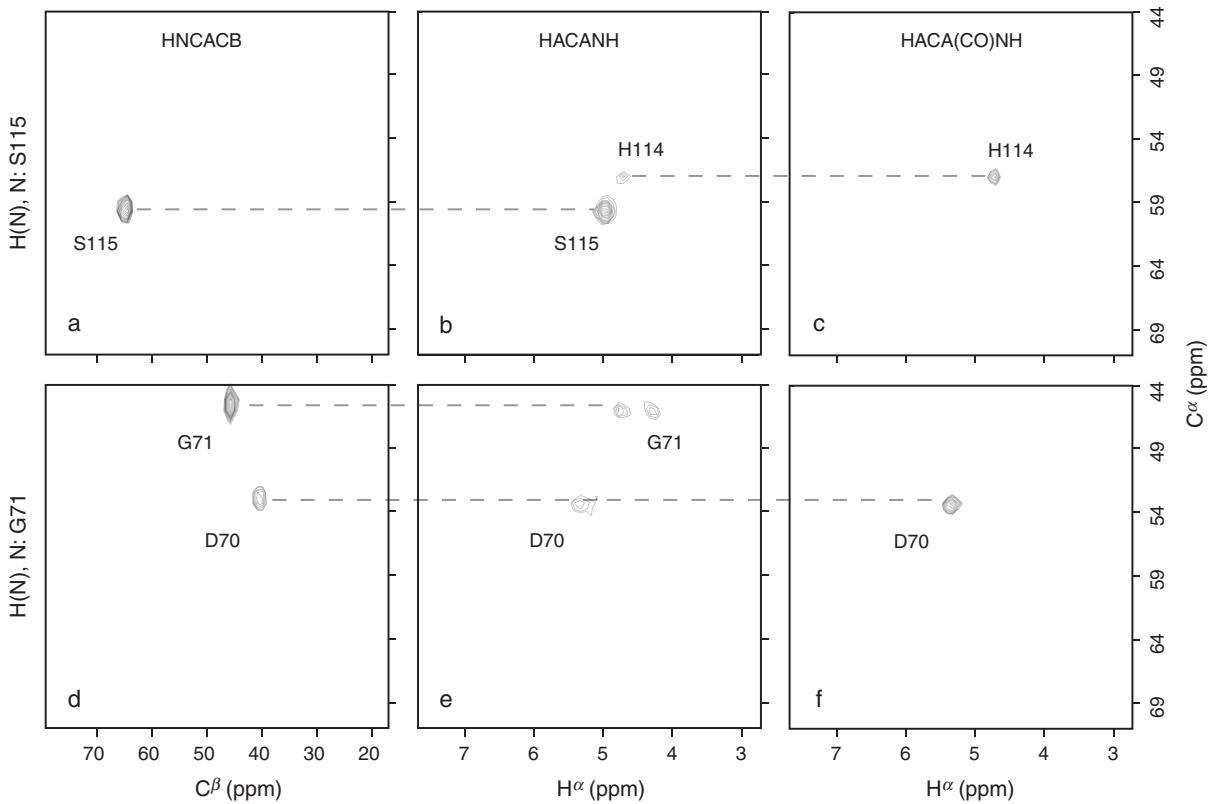

FIGURE 9.14 Projection reconstruction NMR spectra for calbindin D_{28k} (*170*). Shown are 2D slices extracted from (4, 2)D PR (a, d) HNCACB, (b, e) HACANH, and (c, f) HACA(CO)NH spectra recorded using a 0.9 m*M* $^{1}H/^{13}C/^{15}N$ sample of calbindin D_{28k} at 50°C. The spectra were recorded on an 800-MHz NMR spectrometer. The slices correspond to ^{1}H and ^{15}N chemical shifts of residues (a–c) S115 and (d–f) G71. Data were reconstructed to 4D ($64 \times 64 \times 128 \times 738$ complex points) using the HBLV method (bin size = 8) from three orthogonal planes and five tilt angles (eight data sets total).

reconstructed spectrum, do not benefit from the cumulative signal recorded across all of the projections. Thus, the LV algorithm is not optimal when the signal-to-noise ratio for the individual projections is low, as often could be the case for larger proteins. Backprojection (BP), proposed by Kupče and Freeman as a solution to sensitivity problems associated with PR-NMR (*167*), enjoys the benefit of signal accumulation and retains as much signal as would be available from a conventional spectrum recorded for the same length of time as that used to collect the entire set of projections. This reconstruction algorithm was demonstrated by the reconstruction of a 3D HNCO spectrum from 18 projections (*167*). The Hybrid Backprojection-Lower-Value (HBLV) algorithm, introduced subsequently by Venters and coworkers, accumulates signal intensity without significant artifacts and appears particularly useful for the accurate reconstruction of sensitivity-limited data (*170*).

As an illustration of these new approaches for data acquisition and processing, Fig. 9.14 shows 2D slices extracted from (4, 2)D PR HNCACB (Fig. 9.14a, d), HACANH (Fig. 9.14b, e), and HACA(CO)NH (Fig. 9.14c, f) spectra recorded for calbindin D_{28k}. The measuring time for these PR-NMR datasets was ~33 hr.

References

1. L. E. Kay, *J. Magn. Reson.* **173**, 193–207 (2005).
2. V. Tugarinov, P. M. Hwang, L. E. Kay, *Annu. Rev. Biochem.* **73**, 107–146 (2004).
3. R. A. Venters, R. Thompson, J. Cavanagh, *J. Mol. Struct.* **602**, 275–292 (2002).
4. J. Fiaux, E. B. Bertelsen, A. L. Horwich, K. Wüthrich, *Nature* **418**, 207–211 (2002).
5. G. M. Clore, A. M. Gronenborn, *Curr. Opin. Chem. Biol.* **2**, 564–570 (1998).
6. G. M. Clore, A. M. Gronenborn, *Trends. Biotechnol.* **16**, 22–34 (1998).
7. G. M. Clore, A. M. Gronenborn, *Nat. Struct. Biol. (Suppl.)* **4**, 849–853 (1997).
8. P. Permi, *Annu. Rep. NMR Spectrosc.* **53**, 245–296 (2004).
9. R. Riek, G. Wider, K. Pervushin, K. Wüthrich, *Proc. Natl. Acad. Sci. U.S.A.* **96**, 4918–4923 (1999).
10. C. Dalvit, *J. Magn. Reson.* **97**, 645–650 (1992).
11. D. P. Frueh, T. Ito, J. S. Li, G. Wagner, S. J. Glaser, N. Khaneja, *J. Biomol. NMR* **32**, 23–30 (2005).
12. D. T. Browne, G. L. Kenyon, E. L. Packer, H. Sternlicht, D. M. Wilson, *J. Am. Chem. Soc.* **95**, 1316–1323 (1973).
13. T. Yamazaki, W. Lee, C. H. Arrowsmith, D. R. Muhandiram, L. E. Kay, *J. Am. Chem. Soc.* **116**, 11655–11666 (1994).
14. M. A. Markus, K. T. Dayie, P. Matsudaira, G. Wagner, *J. Magn. Reson., Ser. B* **105**, 192–195 (1994).
15. R. A. Venters, C. C. Huang, B. T. Farmer, R. Trolard, L. D. Spicer, C. A. Fierke, *J. Biomol. NMR.* **5**, 339–344 (1995).

16. D. M. LeMaster, *Prog. NMR Spectrosc.* **26**, 371–419 (1994).
17. B. T. Farmer, R. A. Venters, in "Modern Techniques in Protein NMR" (N. R. Krishna, L. J. Berliner, eds.), Vol. 16, pp. 75–120, Kluwer/Plenum, New York, 1998.
18. N. Murali and B.D.N. Rao, *J. Magn. Reson. Ser. A.* **118**, 202–213 (1996).
19. D. M. Kushlan, D. M. LeMaster, *J. Biomol. NMR* **3**, 701–708 (1993).
20. K. H. Gardner, L. E. Kay, *Annu. Rev. Biophys. Biomol. Struct.* **27**, 357–406 (1998).
21. L. E. Kay, K. H. Gardner, *Curr. Opin. Struct. Biol.* **7**, 722–731 (1997).
22. R. A. Venters, B. T. Farmer, C. A. Fierke, L. D. Spicer, *J. Mol. Biol.* **264**, 1101–1116 (1996).
23. D. M. LeMaster, *Meth. Enzymol.* **177**, 23–43 (1989).
24. D. M. LeMaster, *Annu. Rev. Biophys. Biophys. Chem.* **19**, 243–266 (1990).
25. D. Nietlispach, R. T. Clowes, R. W. Broadhurst, Y. Ito, J. H. Keeler, M. Kelly, J. Ashurs, H. Oschkinat, P. J. Domaille, E. D. Laue, *J. Am. Chem. Soc.* **118**, 407–415 (1996).
26. J. Marley, M. Lu, C. Bracken, *J. Biomol. NMR* **20**, 71–75 (2001).
27. T. Torizawa, M. Shimizu, M. Taoka, H. Miyano, M. Kainosho, *J. Biomol. NMR* **30**, 311–325 (2004).
28. T. Szyperski, D. Neri, B. Leiting, G. Otting, K. Wüthrich, *J. Biomol. NMR* **2**, 323–334 (1992).
29. M. K. Rosen, K. H. Gardner, R. C. Willis, W. E. Parris, T. Pawson, L. E. Kay, *J. Mol. Biol.* **263**, 627–636 (1996).
30. N. K. Goto, K. H. Gardner, G. A. Mueller, R. C. Willis, L. E. Kay, *J. Biomol. NMR* **13**, 369–374 (1999).
31. N. K. Goto, L. E. Kay, *Curr. Opin. Struct. Biol.* **10**, 585–592 (2000).
32. S. Rajesh, D. Nietlispach, H. Nakayama, K. Takio, E. D. Laue, T. Shibata, Y. Ito, *J. Biomol. NMR* **27**, 81–86 (2003).
33. K. L. Constantine, L. Mueller, V. Goldfarb, M. Wittekind, W. J. Metzler, J. Yanchunas, J. G. Robertson, M. F. Malley, M. S. Friedrichs, B. T. Farmer, *J. Mol. Biol.* **267**, 1223–1246 (1997).
34. T. Yamazaki, R. Muhandiram, L. E. Kay, *J. Am. Chem. Soc.* **116**, 8266–8278 (1994).
35. K. H. Gardner, L. E. Kay, in "Modern Techniques in Protein NMR" (N. R. Krishna, L. J. Berliner, eds.), Vol. 16, pp. 27–74, Kluwer/Plenum, New York, 1998.
36. V. Tugarinov, R. Muhandiram, A. Ayed, L. E. Kay, *J. Am. Chem. Soc.* **124**, 10025–10035 (2002).
37. F. A. Mulder, A. Ayed, D. Yang, C. H. Arrowsmith, L. E. Kay, *J. Biomol. NMR.* **18**, 173–176 (2000).
38. P. E. Hansen, *Prog. NMR Spectrosc.* **20**, 207–255 (1988).
39. Z. Majerski, M. Zuanic, B. Metelko, *J. Am. Chem. Soc.* **107**, 1721–1726 (1985).
40. D. S. Garrett, Y. J. Seok, D. I. Liao, A. Peterkofsky, A. M. Gronenborn, G. M. Clore, *Biochemistry* **36**, 2517–2530 (1997).
41. K. H. Gardner, M. K. Rosen, L. E. Kay, *Biochemistry* **36**, 1389–1401 (1997).
42. D. M. LeMaster, J. C. LaIuppa, D. M. Kushlan, *J. Biomol. NMR* **4**, 863–870 (1994).
43. D. S. Wishart, B. D. Sykes, F. M. Richards, *J. Mol. Biol.* **222**, 311–333 (1991).
44. D. S. Wishart, B. D. Sykes, *J. Biomol. NMR* **4**, 171–180 (1994).
45. M. Deschamps, I. D. Campbell, *J. Magn. Reson*, **178**, 206–211 (2006).
46. K. Pervushin, B. Vögeli, A. Eletsky, *J. Am. Chem. Soc.* **124**, 12898–12902 (2002).
47. P. Schanda, B. Brutscher, *J. Am. Chem. Soc.* **127**, 8014–8015 (2005).
48. M. Sattler, J. Schleucher, C. Griesinger, *Prog. NMR Spectrosc.* **34**, 93–158 (1999).
49. T. Yamazaki, W. Lee, M. Revington, D. L. Mattiello, F. W. Dahlquist, C. H. Arrowsmith, L. E. Kay, *J. Am. Chem. Soc.* **116**, 6464–6465 (1994).
50. C. Bracken, A. G. Palmer, J. Cavanagh, *J. Biomol. NMR* **9**, 94–100 (1997).
51. H. Matsuo, E. Kupče, H. Li, G. Wagner, *J. Magn. Reson.* **111**, 194–198 (1996).

52. Z. Y. Sun, D. P. Frueh, P. Selenko, J. C. Hoch, G. Wagner, *J. Biomol. NMR* **33**, 43–50 (2005).
53. P. Permi, A. Annila, *J. Biomol. NMR* **20**, 127–133 (2001).
54. A. Meissner, O. W. Sørensen, *J. Magn. Reson.* **150**, 100–104 (2001).
55. D. Nietlispach, Y. Ito, E. D. Laue, *J. Am. Chem. Soc.* **124**, 11199–11207 (2002).
56. B. A. Lyons, M. Tashiro, L. Cedergren, B. Nilsson, G. T. Montelione, *Biochemistry* **32**, 7839–7845 (1993).
57. B. T. Farmer, R. A. Venters, *J. Am. Chem. Soc.* **117**, 4187–4188 (1995).
58. P. Tsang, P. E. Wright, M. Rance, *J. Am. Chem. Soc.* **112**, 8183–8185 (1990).
59. R. A. Venters, W. J. Metzler, L. D. Spicer, L. Mueller, B. T. Farmer, *J. Am. Chem. Soc.* **117**, 9592–9593 (1995).
60. S. Grzesiek, P. Wingfield, S. Stahl, D. Kaufman, A. Bax, *J. Am. Chem. Soc.* **117**, 9594–9595 (1995).
61. C. Zwahlen, K. H. Gardner, S. P. Sarma, D. A. Horita, R. A. Byrd, L. E. Kay, *J. Am. Chem. Soc.* **120**, 7617–7625 (1998).
62. D. R. Muhandiram, G. Y. Xu, L. E. Kay, *J. Biomol. NMR* **3**, 463–470 (1993).
63. Z. Zolnai, N. Juranic, S. Macura, *J. Biomol. NMR* **3**, 463–470 (1993).
64. V. Tugarinov, R. Sprangers, L. E. Kay, *J. Am. Chem. Soc.* **126**, 4921–4925 (2004).
65. V. Tugarinov, L. E. Kay, *J. Am. Chem. Soc.* **125**, 13868–13878 (2003).
66. G. A. Mueller, W. Y. Choy, D. Yang, J. D. Forman-Kay, R. A. Venters, L. E. Kay, *J. Mol. Biol.* **300**, 197–212 (2000).
67. V. Tugarinov, W. Y. Choy, V. Y. Orekhov, L. E. Kay, *Proc. Natl. Acad. Sci. U.S.A.* **102**, 622–627 (2005).
68. B. O. Smith, Y. Ito, A. Raine, S. Teichman, L. ben-Tovim, D. Nietlispach, R. W. Broadhurst, T. Terada, M. Kelly, H. Oschkinat, T. Shibata, S. Yokoyama, E. D. Laue, *J. Biomol. NMR* **8**, 360–368 (1996).
69. G. M. Clore, M. R. Starich, C. A. Bewley, M. Cai, J. Kuszewski, *J. Am. Chem. Soc.* **121**, 6513–6514 (1999).
70. A. Medek, E. T. Olejniczak, R. P. Meadows, S. W. Fesik, *J. Biomol. NMR* **18**, 229–238 (2000).
71. A. J. Wand, J. H. Short, *Meth. Enzymol.* **239**, 700–717 (1994).
72. G. M. Clore, A. M. Gronenborn, *Prog. Biophys. Mol. Biol.* **62**, 153–184 (1994).
73. G. M. Clore, A. M. Gronenborn, *Crit. Rev. Biochem. Mol. Biol.* **30**, 351–385 (1995).
74. T. Härd, *Q. Rev. Biophys.* **32**, 57–98 (1999).
75. A. M. Petros, S. W. Fesik, *Meth. Enzymol.* **239**, 717–739 (1994).
76. H. Wu, L. D. Finger, J. Feigon, *Meth. Enzymol.* **394**, 525–545 (2005).
77. E. R. Zuiderweg, *Biochemistry* **41**, 1–7 (2002).
78. A. J. Wand, S. W. Englander, *Curr. Opin. Biotechnol.* **7**, 403–408 (1996).
79. D. Nietlispach, H.R. Mott, K.M. Stott, P.R. Nielsen, A. Thiru, E. D. Laue, in "Protein NMR Techniques" (A. K. Downing, ed.), Vol. 278, pp. 255–288, Humana Press Inc., Totowa, NJ, 2005.
80. D. E. Wemmer, P. G. Williams, *Meth. Enzymol.* **239**, 739–767 (1994).
81. T. Carlomagno, *Annu. Rev. Biophys. Biomol. Struct.* **34**, 245–266 (2005).
82. S. W. Homans, *Angew. Chem. Int. Ed. Engl.* **343**, 290–300 (2004).
83. M. Pellecchia, D. S. Sem, K. Wüthrich, *Nat. Rev. Drug Discov.* **1**, 211–219 (2002).
84. L. Y. Lian, I. L. Barsukov, M. J. Sutcliffe, K. H. Sze, G. C. Roberts, *Meth. Enzymol.* **239**, 657–700 (1994).
85. C. Dominguez, R. Boelens, A. M. Bonvin, *J. Am. Chem. Soc.* **125**, 1731–1737 (2003).
86. U. Schiebor, M. Vogtherr, B. Elshorst, M. Betz, S. Grimme, B. Pescatore, T. Langer, K. Saxena, H. Schwalbe, *ChemBioChem* **6**, 1891–1898 (2005).

87. S. B. Shuker, P. J. Hajduk, R. P. Meadows, S. W. Fesik, *Science* **274**, 1531–1534 (1996).
88. B. T. Farmer, K. L. Constantine, V. Goldfarb, M. S. Friedrichs, M. Wittekind, J. Yanchunas, J. G. Robertson, L. Mueller, *Nat. Struct. Biol.* **3**, 995–997 (1996).
89. L. Fielding, *Tetrahedron* **56**, 6151–6170 (2000).
90. C. S. Wilcox, in "Frontiers in Supramolecular Organic Chemistry and Photochemistry" (H.-J. Schneider, H. Dürr, eds.), pp. 123–143, VCH Verlag, Weinheim, 1991.
91. H. Takahashi, T. Nakanishi, K. Kami, Y. Arata, I. Shimada, *Nat. Struct. Biol.* **7**, 220–223 (2000).
92. V. Dötsch, *Meth. Enzymol.* **339**, 343–357 (2001).
93. M. Allen, L. Varani, G. Varani, *Meth. Enzymol.* **339**, 357–376 (2001).
94. J. Qin, O. Vinogradova, A. M. Gronenborn, *Meth. Enzymol.* **339**, 377–389 (2001).
95. Ē. Kupče, R. Freeman, *J. Magn. Reson., Ser. A* **115**, 273–276 (1995).
96. R. Fu, G. Bodenhausen, *Chem. Phys. Lett.* **245**, 415–420 (1995).
97. R. Fu, G. Bodenhausen, *J. Magn. Reson., Ser. A* **117**, 324–325 (1995).
98. H. Takahashi, Miyazawa, Y. Ina, Y. Fukunishi, Y. Mizukoshi, H. Nakamura, I. Shimada, *J. Biomol. NMR*, **34**, 167–177 (2006).
99. G. M. Clore, A. M. Gronenborn, *J. Magn. Reson.* **48**, 402–417 (1982).
100. G. M. Clore, A. M. Gronenborn, *J. Magn. Reson.* **53**, 423–442 (1983).
101. N. R. Nirmala, G. M. Lippens, K. Hallenga, *J. Magn. Reson.* **100**, 25–42 (1992).
102. G. M. Lippens, C. Cerf, K. Hallenga, *J. Magn. Reson.* **99**, 268–281 (1992).
103. T. Polenova, T. Iwashita, A. G. Palmer, A. E. McDermott, *Biochemistry* **36**, 14202–14217 (1997).
104. N. U. Jain, T. J. Wyckoff, C. R. Raetz, J. H. Prestegard, *J. Mol. Biol.* **343**, 1379–1389 (2004).
105. G. M. Clore, C. D. Schwieters, *J. Am. Chem. Soc.* **125**, 2902–2912 (2003).
106. M. A. McCoy, D. F. Wyss, *J. Am. Chem. Soc.* **124**, 2104–2105 (2002).
107. F. Lohr, G. N. Yalloway, S. G. Mayhew, H. Rüterjans, *ChemBioChem.* **5**, 1523–1534 (2004).
108. A. L. Breeze, *Prog. NMR Spectrosc.* **36**, 323–372 (2000).
109. G. Otting, K. Wüthrich, *Q. Rev. Biophys.* **23**, 39–96 (1990).
110. R. H. Griffey, A. G. Redfield, *J. Magn. Reson.* **65**, 344–348 (1985).
111. R. H. Griffey, A. G. Redfield, *Q. Rev. Biophys.* **19**, 51–82 (1987).
112. G. Otting, H. Senn, G. Wagner, K. Wüthrich, *J. Magn. Reson.* **70**, 500–505 (1986).
113. H. Senn, G. Otting, K. Wüthrich, *J. Am. Chem. Soc.* **109**, 1090–1092 (1987).
114. M. A. Weiss, A. G. Redfield, R. H. Griffey, *Proc. Natl. Acad. Sci. U.S.A* **83**, 1325–1329 (1986).
115. S. W. Fesik, R. T. Gampe, T. W. Rockway, *J. Magn. Reson.* **74**, 366–371 (1987).
116. A. Bax, M. A. Weiss, *J. Magn. Reson.* **71**, 571–575 (1987).
117. G. Wider, C. Weber, R. Traber, H. Widmer, K. Wüthrich, *J. Am. Chem. Soc.* **112**, 9015–9016 (1990).
118. M. Ikura, A. Bax, *J. Am. Chem. Soc.* **114**, 2433–2440 (1992).
119. A. M. Petros, M. Kawai, J. R. Luly, S. W. Fesik, *FEBS Lett.* **308**, 309–314 (1992).
120. C. Weber, G. Wider, B. von Freyberg, R. Traber, W. Braun, H. Widmer, K. Wüthrich, *Biochemistry* **30**, 6563–6574 (1991).
121. P. J. M. Folkers, R. H. A. Folmer, R. N. H. Konings, C. W. Hilbers, *J. Am. Chem. Soc.* **115**, 3798–3799 (1993).
122. R. Freeman, T. H. Mareci, G. A. Morris, *J. Magn. Reson.* **42**, 341–345 (1981).
123. G. Wider, C. Weber, K. Wüthrich, *J. Am. Chem. Soc.* **113**, 4676–4678 (1991).
124. M. Rance, P. E. Wright, B. A. Messerle, L. D. Field, *J. Am. Chem. Soc.* **109**, 1591–1593 (1987).

125. G. Gemmecker, E. T. Olejniczak, S. W. Fesik, *J. Magn. Reson.* **96**, 199–204 (1992).
126. Ē. Kupče, R. Freeman, *J. Magn. Reson.* **127**, 36–48 (1997).
127. C. Zwahlen, P. Legault, S. F. J. Vincent, J. Greenblatt, R. Konrat, L. E. Kay, *J. Am. Chem. Soc.* **119**, 6711–6721 (1997).
128. A. C. Stuart, K. A. Borzilleri, J. M. Withka, A. G. Palmer, *J. Am. Chem. Soc.* **121**, 5346–5347 (1999).
129. W. Lee, M. J. Revington, C. Arrowsmith, L. E. Kay, *FEBS Lett.* **350**, 87–90 (1994).
130. Y. Xia, A. Yee, C. H. Arrowsmith, X. Gao, *J. Biomol. NMR* **27**, 193–203 (2003).
131. H. S. Atreya, T. Szyperski, *Meth. Enzymol.* **394**, 78–108 (2005).
132. J. Chen, V. A. Mandelshtam, A. J. Shaka, *J. Magn. Reson.* **146**, 363–368 (2000).
133. V. A. Mandelshtam, *J. Magn. Reson.* **144**, 343–356 (2000).
134. H. Hu, A. A. De Angelis, V. A. Mandelshtam, A. J. Shaka, *J. Magn. Reson.* **144**, 357–366 (2000).
135. L. Frydman, A. Lupulescu, T. Scherf, *J. Am. Chem. Soc.* **125**, 9204–9217 (2003).
136. L. Frydman, T. Scherf, A. Lupulescu, *Proc. Natl. Acad. Sci. U.S.A.* **99**, 15858–15862 (2002).
137. R. Freeman, Ē. Kupče, *J. Magn. Reson.* **163**, 56–63 (2003).
138. R. Freeman, Ē. Kupče, *J. Magn. Reson.* **162**, 158–165 (2003).
139. R. Freeman, Ē. Kupče, *J. Magn. Reson.* **162**, 300–310 (2003).
140. R. Freeman, Ē. Kupče, *J. Biomol. NMR* **27**, 101–113 (2003).
141. R. Freeman, Ē. Kupče, *Concepts Magn. Reson.* **23A**, 63–75 (2004).
142. D. Rovnyak, J. C. Hoch, A. S. Stern, G. Wagner, *J. Biomol. NMR* **30**, 1–10 (2004).
143. D. Marion, *J. Biomol. NMR* **32**, 141–150 (2005).
144. T. Luan, V. Jaravine, A. Yee, C. H. Arrowsmith, V. Y. Orekhov, *J. Biomol. NMR* **33**, 1–14 (2005).
145. V. Tugarinov, L. E. Kay, I. Ibraghimov, V. Y. Orekhov, *J. Am. Chem. Soc.* **127**, 2767–2775 (2005).
146. S. Kim, T. Szyperski, *J. Am. Chem. Soc.* **125**, 1385–1393 (2003).
147. T. Szyperski, G. Wider, J. H. Bushweller, K. Wüthrich, *J. Am. Chem. Soc.* **115**, 9307–9308 (1993).
148. T. Szyperski, G. Wider, J. H. Bushweller, K. Wüthrich, *J. Biomol. NMR* **3**, 127–132 (1993).
149. K. Ding, A. M. Gronenborn, *J. Magn. Reson.* **156**, 262–268 (2002).
150. J. P. Simorre, B. Brutscher, M. S. Caffrey, D. Marion, *J. Biomol. NMR* **4**, 325–333 (1994).
151. B. Brutscher, J. P. Simorre, M. S. Caffrey, D. Marion, *J. Magn. Reson.* **105**, 77–82 (1994).
152. T. Szyperski, D. C. Yeh, D. K. Sukumaran, H. N. Moseley, G. T. Montelione, *Proc. Natl. Acad. Sci. U.S.A.* **99**, 8009–8014 (2002).
153. B. Bersch, E. Rossy, J. Coves, B. Brutscher, *J. Biomol. NMR* **27**, 57–67 (2003).
154. W. Kozminski, I. Zhukov, *J. Biomol. NMR* **26**, 157–166 (2003).
155. F. Lohr, H. Rüterjans, *J. Biomol. NMR* **6**, 189–197 (1995).
156. H. S. Atreya, T. Szyperski, *Proc. Natl. Acad. Sci. U.S.A.* **101**, 9642–9647 (2004).
157. Y. Shen, H. S. Atreya, G. Liu, T. Szyperski, *J. Am. Chem. Soc.* **127**, 9085–9099 (2005).
158. H. S. Atreya, A. Eletsky, T. Szyperski, *J. Am. Chem. Soc.* **127**, 4554–4555 (2005).
159. Y. Xia, G. Zhu, S. Veeraraghavan, X. Gao, *J. Biomol. NMR* **29**, 467–476 (2004).
160. G. Liu, J. Aramini, H. S. Atreya, A. Eletsky, R. Xiao, T. A. Acton, L. C. Ma, G. T. Montelione, T. Szyperski, *J. Biomol. NMR* **32**, 261–261 (2005).
161. G. Liu, Y. Shen, H. S. Atreya, D. Parish, Y. Shao, D. Sukumaran, R. Xiao, A. Yee, A. Lemak, A. Bhattacharya, T. A. Acton, C. H. Arrowsmith, G. T. Montelione, T. Szyperski, *Proc. Natl. Acad. Sci., U.S.A.* **102**, 10487–10492 (2005).
162. R. Freeman, Ē. Kupče, *J. Biomol. NMR* **25**, 349–354 (2003).

163. R. Freeman, Ē. Kupče, *J. Biomol. NMR* **27**, 383–387 (2003).
164. R. Freeman, Ē. Kupče, *J. Am. Chem. Soc.* **125**, 13958–13959 (2003).
165. R. Freeman, Ē. Kupče, *J. Am. Chem. Soc.* **126**, 6429–6440 (2004).
166. R. Freeman, Ē. Kupče, *J. Biomol. NMR* **28**, 391–395 (2004).
167. Ē. Kupče, R. Freeman, *Concepts Magn. Reson.* **22A**, 4–11 (2004).
168. Ē. Kupče, R. Freeman, *J. Magn. Reson.* **172**, 329–332 (2005).
169. B. E. Coggins, R. A.Venters, P. Zhou, *J. Am. Chem. Soc.* **126**, 1000–1001 (2004).
170. R. A. Venters, B. E. Coggins, D. Kojetin, J. Cavanagh, P. Zhou, *J. Am. Chem. Soc.* **127**, 8785–8795 (2005).